Updating nonlinear stochastic dynamics of an uncertain nozzle model using probabilistic learning with partial observability and incomplete dataset

Evangéline Capiez-Lernout, Olivier Ezvan, Christian Soize

Updating Nonlinear Stochastic Dynamics of an Uncertain Nozzle Model using Probabilistic Learning with Partial Observability and Incomplete dataset

Evangéline Capiez-Lernout[a], Olivier Ezvan[a], Christian Soize[a,*]

[a] *Université Gustave Eiffel, MSME UMR 8208, 5 bd Descartes, 77454 Marne-la-Vallée, France*

Abstract

This paper introduces a methodology for updating the nonlinear stochastic dynamics of a nozzle with uncertain computational model. The approach focuses on a high-dimensional nonlinear computational model constrained by a small target dataset. Challenges include the large number of degrees-of-freedom, geometric nonlinearities, material uncertainties, stochastic external loads, under-observability, and high computational costs. A detailed dynamic analysis of the nozzle is presented. An updated statistical surrogate model relating the observations of interest to the control parameters is constructed. Despite small training and target datasets, and partial observability, the study successfully applies Probabilistic Learning on Manifolds (PLoM) to address these challenges. PLoM captures geometric nonlinear effects and uncertainty propagation, improving conditional mean statistics compared to training data. The conditional confidence region demonstrates the ability of the methodology to accurately represent both observed and unobserved output variables, contributing to advancements in modeling complex systems.

Keywords: Probabilistic learning, uncertainty quantification, nonlinear stochastic dynamics, surrogate model, partial information, statistical inverse problem, nozzle, machine learning for engineering applications

Nomenclature

$\mathbb{R}$: set of real numbers.
$\mathbb{R}^n$: Euclidean vector space on $\mathbb{R}$ of dimension n.
$\mathbb{M}_{n,m}$: set of $(n \times m)$ real matrices.
$\mathbb{M}_n$: set of $(n \times n)$ real matrices.
$\mathbb{M}_n^+$: set of positive-definite $(n \times n)$ real matrices.
$[I_n]$: identity matrix in $\mathbb{M}_n$.
$\langle \mathbf{x}, \mathbf{y} \rangle$: inner product in $\mathbb{R}^n$.
$\| \mathbf{x} \|$: norm in $\mathbb{R}^n$ such that $\| \mathbf{x} \| = \langle \mathbf{x}, \mathbf{x} \rangle$.
$[x]^T$: transpose of matrix $[x]$.
$\| [x] \|$: Frobenius norm of matrix $[x]$.
$\delta_{kk'}$: Kronecker's symbol.

$\mathcal{D}_{\text{targ}}$: target dataset.
$\mathcal{D}_{\text{train}}$: training dataset.
$\mathcal{D}_{\text{learn}}$: learning dataset.
$\mathbb{E}$: mathematical expectation operator.
n_d: number of points in the training data set.
n_{o}: identification-observation vector dimension.
n_w: dimension of the control parameter.
$\mathbf{w}$: vector of control parameters.
N_r: target vector dimension.
N_{o}: observation vector dimension.
N_{ud}: number of points in the learning dataset.
$\mathbf{O}$: Random observation in $\mathbb{R}^{N_{\text{o}}}$.
$\mathbf{O}_{\text{id}}$: Random identification observation in $\mathbb{R}^{n_{\text{o}}}$.
$\mathbf{O}_{\text{ud}}$: Updated random observation in $\mathbb{R}^{N_{\text{o}}}$.
$\mathbf{U}$: random vector of uncontrolled parameter.
$\mathbb{Y}(t, \mathbf{w})$: random displacement of observation.

ISDE: Itô Stochastic Differential Equation.
pdf: probability density function.
psd: power spectral density.

*Corresponding author: C. Soize, christian.soize@univ-eiffel.fr
Email addresses: evangeline.capiez-lernout@univ-eiffel.fr (Evangéline Capiez-Lernout), olivier.ezvan@univ-eiffel.fr (Olivier Ezvan), christian.soize@univ-eiffel.fr (Christian Soize)

Published in ASME Journal of Computing and Information Science in Engineering, 2024 *March 31, 2024*

1. Introduction

Numerous works have highlighted the significance of nozzles concerning the flow analyses (see for instance [1, 2, 3]), the jet noise source and acoustics (see for instance [4, 5, 6, 7, 8]), the nozzle materials [9, 10, 11], the nozzle vibrations [12], the fluid-structure interactions and vibroacoustics [13, 14, 15, 16], the nozzle optimization [17, 18, 19, 20, 21, 22]. The effects of uncertainties in nozzle models have also been studied, see for instance [23, 24, 25, 26]. It should be noted that vibrations and structural dynamic analyses of nozzle structures are important aspects of aerospace engineering. However, only few works have been published in this field, in particular for nonlinear stochastic dynamics of nozzle structures. This paper has two main objectives. The first one is to present a detailed analysis of a challenging problem consisting in updating the nonlinear stochastic dynamics of a nozzle with model uncertainties, with partial observability, and with limited data. The second one is the methodology that is proposed for analyzing this challenging problem.

More precisely, the paper proposes a methodology dedicated to the updating of control parameters within high-dimensional computational models constrained by an incomplete target dataset due to limited data. Note that the methodology proposed for solving such a problem holds significant interest across various industrial sectors, including automotive, aeronautics, and aerospace engineering. In the present work, the difficulties associated with nozzles, which are thin composite structures exposed to external time-dependent excitations, fall within this framework. Here, the complexity of this computational problem arises (1) from the large number of degrees-of-freedom of the computational model, (2) from the geometric nonlinear effects in dynamics, induced by displacements comparable to the nozzle thickness, (3) from the presence of model uncertainties in the representation of homogenized materials, (4) from the stochastic external load due the nozzle excitation, (5) from the under-observability and the limited data for solving the statistical inverse problem required for the updating, and (6) the high-computational cost for constructing one realization of the responses of the nonlinear dynamical system. Such parameterized computational stochastic model will be meticulously constructed, allowing for computing accurate statistics of output observations.

As explained above, the inherent complexity of this problem results in substantial computational costs yielding a partial observability of the nonlinear dynamical behavior of the structure with respect to its control parameters. As a consequence, we have to solve the problem for which only a small training dataset is available. The updating of the nonlinear uncertain stochastic computational model is carried out with respect to a given target dataset that is constituted of an incomplete data, for instance, for the case of a limited number of sensors. To address such issues, it is then necessary to develop surrogate models for these parameterized high-dimensional computational models.

Note that the nozzle presents a structural complexity. Its small thickness requires a fine finite element mesh with numerous degrees of freedom. Model uncertainties within the structural system arise from a uncontrolled parameter, while the external load, represented by a stationary stochastic process depending on the control parameter, has a sufficiently high intensity for triggering a nonlinear response. Since the external load is a stationary stochastic process, we are interested in constructing the stationary random displacements responses by solving a set of nonlinear stochastic coupled differential equations in the time domain, involving multiple time steps. In addition, the nonlinear nature of the dynamical system requires to use iterative algorithms for each time step, which is particularly time consuming. The observations of interest, expressed as displacement amplitudes in the frequency domain, are obtained at the nozzle exit.

In the context of constructing an updated surrogate model, numerous possibilities and methodologies have been proposed in the literature. For instance, there are efficient scientific machine learning techniques for sampling distributions on manifolds [27, 28, 29, 30, 31, 32, 33, 34, 35, 36, 37]. Considering the specificities of the problem at hand – namely, the construction of a statistical surrogate model from a small training dataset for the updated nonlinear stochastic dynamical system with under-observability and incomplete data – there are various tools available. Note that the problem under consideration requires to solve a statistical inverse problem with constraints defined by the target. In this paper, we propose the use of Probabilistic Learning on Manifolds (PLoM) [32, 38] under constraints [39, 40]. The PLoM algorithm is particularly well-suited for scenarios involving small training datasets, and its efficiency has been demonstrated across various domains. Examples include non-convex optimization under uncertainty [41, 42, 43, 44], model-form uncertainties using random bases [45], and the updating, design, and control of dynamical systems [46, 47, 48]. The statistical surrogate model will be based on conditional statistics for given control parameter, using the learned realizations obtained from PLoM under the constraints defined by the target. This statistical surrogate model reduces the distance between the updated observations and the available target data, for each

given value of the control parameter.

The manuscript is organized as follows. Section 2 is devoted to the nozzle dynamics and introduces the parameterized uncertain stochastic computational model of the nonlinear dynamical system. Following this, Section 3 meticulously constructs the prior probability models. This encompasses the stationary stochastic process that defines the external load, the control parameter employed in the probabilistic learning updating process, and the uncontrolled parameter that capture all sources of model uncertainties. Sections 4 and 5 are devoted to the definition of the training and target datasets. Section 6 deals with the construction of the learned dataset under constraints. Section 7 addresses the computational challenges that are essential for a better understanding of related physics and for obtaining a predictive computational model through algorithm optimization. The considered numerical finite element model of the nozzle and its related modal properties are presented in Sections 8 and 9. The numerical construction of the stochastic external load is detailed in Section 10 and the numerical values allowing for a complete description of the training and target datasets are given in Section 11. Section 12 conducts a convergence analysis of the PLoM algorithm used for the updated statistical surrogate model. Finally, Section 13 presents and discusses the learning results that validate the updating process. The PLoM algorithm is briefly summarized in Appendix A.

To aid in the comprehension of this paper, Figure 1 presents a simplified flowchart of the main steps of the methodology used, referencing the relevant sections and equations.

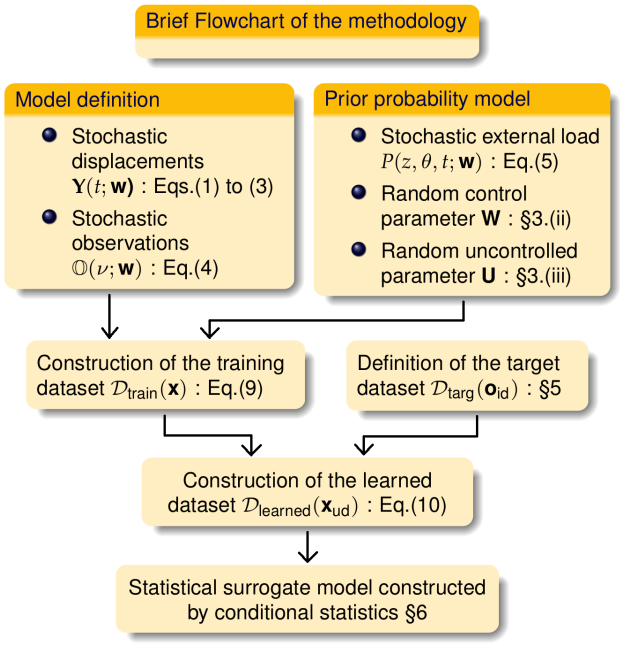

Figure 1: Flowchart summarizing the main steps of the methodology.

2. Parameterized nonlinear uncertain stochastic dynamical computational model for the nozzle

The present paper is devoted to the nonlinear stochastic dynamics of a three-dimensional nozzle for which geometric nonlinearities are taken into account with an elastic material and for which the external load is a stochastic process.

The nozzle is designed so as to get a subsonic acceleration of the gas from the combustion chamber until the throat, where the gas velocity presents a Mach number of one. The flow is then accelerated supersonically by providing a path of increasing flow area. The external load is intrinsically linked to the noise emanating from the turbulent, high-velocity gas jet. Consequently, an appropriate approach involves modeling the external loading via a stochastic

process. Considering the intensity of such a nozzle jet in conjunction with the slender nozzle thickness, it is conceivable that the vibrational behavior at the nozzle exit may manifest as vibrational amplitudes operating within the domain of geometric nonlinearities. Figure 2 shows the finite element mesh of the nozzle structure that is considered.

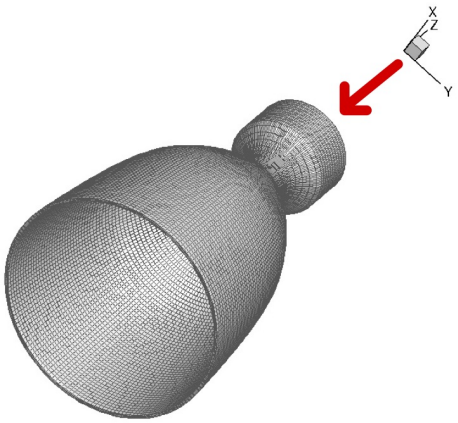

Figure 2: Finite element mesh of the nozzle. The red arrow indicates the inlet section and the flow direction.

The nozzle structure under consideration is made up of a linear elastic material and is assumed to undergo large displacements yielding geometrically nonlinear effects. The nozzle structure is fixed at the beginning of the combustion chamber and is subjected to a parameterized stochastic pressure field representing the turbulent gas jet at the inner wall of the nozzle. There is also uncertainty in the constitutive equation. A total Lagrangian formulation is chosen, allowing the dynamical equations to be expressed around a reference configuration taken as an equilibrium state.

The finite element discretization yields a high-dimensional nonlinear uncertain stochastic computational model with n_y degrees of freedom that is formulated in the time domain. The stochastic excitation is parameterized as a function of a control parameter denoted by the $\mathbb{R}^{n_w}$-vector $\mathbf{w}$ defined in $C_w \subset \mathbb{R}^{n_w}$. As a consequence, the finite element force vector, for a given value of the control parameter $\mathbf{w} \in C_w$, is represented by the $\mathbb{R}^{n_y}$-valued stochastic process $\{\mathbf{F}(t;\mathbf{w}), t \in T\}$, in which $T =]t_0, t_f] \subset \mathbb{R}$. It is assumed to be modeled as a stationary stochastic process. The uncertainties in the constitutive equation are represented by an uncontrolled random parameter represented by the $\mathbb{R}^{n_u}$-valued random vector $\mathbf{U}$ whose probability distribution support is $C_u \subset \mathbb{R}^{n_u}$. The stochastic response is thus represented by the $\mathbb{R}^{n_y}$-valued stochastic process $\mathbf{Y}(t;\mathbf{w})$ indexed by $T \subset \mathbb{R}$ and that depends on control parameter $\mathbf{w}$. Note that it also depends on stochastic excitation vector $\mathbf{F}(t;\mathbf{w})$ and of uncontrolled parameter $\mathbf{U}$, but it is chosen to omit it for clarity of notation. Stochastic process $\mathbf{Y}(t;\mathbf{w})$ indexed by $T \subset \mathbb{R}$ and that depends on control parameter $\mathbf{w}$ is then the solution of the parameterized stochastic nonlinear dynamical initial-value problem that is written as

$$[M]\,\ddot{\mathbf{Y}}(t;\mathbf{w}) + [D]\,\dot{\mathbf{Y}}(t;\mathbf{w}) + [K(\mathbf{U})]\,\mathbf{Y}(t;\mathbf{w}) + \mathbf{f}^{\mathrm{NL}}\big(\mathbf{Y}(t;\mathbf{w}),\mathbf{U}\big) = \mathbf{F}(t;\mathbf{w}) \quad , \quad \forall t \in T, \tag{1}$$

$$\mathbf{Y}(t_0;\mathbf{w}) = \mathbf{Y}_0(\mathbf{w},\mathbf{U})\,, \tag{2}$$

$$\dot{\mathbf{Y}}(t_0;\mathbf{w}) = \mathbf{Y}_1(\mathbf{w},\mathbf{U})\,. \tag{3}$$

In Eq. (1), the mass matrix $[M]$ is a $(n_y \times n_y)$ real symmetric positive-definite matrix and is deterministic. The damping and linear elastic stiffness matrices $[D]$ and $[K(\mathbf{U})]$ are random matrices with values in the set of the $(n_y \times n_y)$ real symmetric positive-definite matrices. Note that damping matrix $[D]$ results from a Rayleigh model. The $\mathbb{R}^{n_y}$-valued random vector $\mathbf{f}^{\mathrm{NL}}(\mathbf{Y}(t;\mathbf{w}),\mathbf{U})$ corresponds to the nonlinear uncertain internal forces at a given time t and the $\mathbb{R}^{n_y}$-valued stochastic process $\{\mathbf{F}(t;\mathbf{w}), t \in T\}$ is issued from the modeling of the turbulent gas jet that will be described in Section 11. It should be noted that the $\mathbb{R}^{n_y}$-valued random vectors $\mathbf{Y}_0(\mathbf{w},\mathbf{U})$ and $\mathbf{Y}_1(\mathbf{w},\mathbf{U})$ are obtained from a previous nonlinear stochastic computation on $T_0 =]0, t_0]$ for which the initial conditions defined by Eqs. (2), (3) are replaced by null initial conditions. Namely, denoting by $\{\mathbf{Y}^0(t;\mathbf{w}), t \in T_0\}$ the random response of such an initial-value

problem, we have $\mathbf{Y}_0(\mathbf{w}, \mathbf{U}) = \mathbf{Y}^0(t_0; \mathbf{w})$ and $\mathbf{Y}_1(\mathbf{w}, \mathbf{U}) = \dot{\mathbf{Y}}^0(t_0; \mathbf{w})$. Indeed, note that two distinct stochastic nonlinear dynamical initial-value problems have to be computationally solved in order to ensure the stationarity of the random response.

The nonlinear stochastic uncertain computational model allows for obtaining the whole displacement response $\mathbf{Y}(t; \mathbf{w})$ as a function of time. Nevertheless, in the present nozzle context, it is assumed that we deal with an under-observed situation for which it is assumed that only the bending displacement response located at the outer radius of the nozzle exit is available. The relevance for such a choice of location defining the under-observability is related to the nozzle exit undergoing the largest displacements under bending motion reflecting nozzle swelling, due to its bell geometry. Moreover, the thin thickness of the nozzle yields normal displacements with little variation in the nozzle shell thickness. It should also be noted that although the presence of nonlinearities couples the axial and bending motions of the nozzle, the bending response is of greater importance. Such an under-observed situation yields the introduction of partial observation $\mathbb{Y}(t; \mathbf{w})$ that is represented by the $\mathbb{R}^{\overline{n}_y}$-valued random vector $\mathbb{Y}(t; \mathbf{w}) = O(\mathbf{Y}(t; \mathbf{w}))$ at a given time t with $\overline{n}_y \ll n_y$ and that corresponds to the normal bending displacements located at the outer radius of the nozzle exit. We aim to predict observations in the frequency domain, using N_ν sampling frequencies belonging to a finite set denoted as $\mathcal{F}$ corresponding to a specified frequency band in Hz. This is represented by the random vector $\mathbf{O}$, which encompasses the random family $\{\mathbb{O}(\nu; \mathbf{w}), \nu \in \mathcal{F}\}$. Here, $\mathbb{O}(\nu; \mathbf{w})$ is an $\mathbb{R}^{\overline{n}_y}$-valued random variable defined by

$$\mathbb{O}(\nu; \mathbf{w}) = \log\left(|\widehat{\mathbb{Y}}(2\pi\nu; \mathbf{w})|\right) \quad , \quad \nu \in \mathcal{F} \quad , \tag{4}$$

in which $\nu \mapsto \widehat{\mathbb{Y}}(2\pi\nu; \mathbf{w})$ is the Fourier transform of partial observation $t \mapsto \mathbb{Y}(t; \mathbf{w})$. The identification observation is defined as the random vector $\mathbf{O}_{\text{id}}$ representing the random family $\{\mathbb{O}_{\text{id}}(\nu; \mathbf{w}), \nu \in \mathcal{F}\}$, which corresponds to a subset of observation vector $\mathbf{O}$, and which is such that $\mathbb{O}_{\text{id}}(\nu; \mathbf{w}) = [B]\mathbb{O}(\nu; \mathbf{w})$, where $[B]$ is a $(n_{\text{exp}} \times \overline{n}_y)$ observation matrix. Its entries are related to the indices corresponding to sensor location of available measurements. It then constitutes an incomplete dataset for the target from which the updating (probabilistic learning under constraints) will be performed.

3. Prior probability model

There are uncertainties in the computational model, modeled by the random vector $\mathbf{U}$, which is an uncontrolled parameter. The computational model is stochastic, due to the stochastic load vector that depends on a stochastic process $G = \{G(t; \mathbf{w}), t \in \mathbb{R}\}$. This stochastic uncertain computational model depends on a control parameter $\mathbf{w}$. In order to construct the statistical surrogate model of quantities of interest with respect to control parameter $\mathbf{w}$, using the probabilistic learning, vector $\mathbf{w}$ is modeled by a vector-valued random variable $\mathbf{W}$. In this Section, we define the prior probability models of stochastic process G, and of random vectors $\mathbf{W}$ and $\mathbf{U}$. It is assumed that $\mathbf{U}$ is statistically independent of G and $\mathbf{W}$.

(i) Prior probability model of G. The stochastic load vector $\mathbf{F}(t; \mathbf{w})$ corresponds to the finite element discretization of a positive pressure load representing the gas jet at the wall of the nozzle. The pressure flow is constituted of an axisymmetric mean pressure flow that is overlaid with a positive statistical fluctuation that depends on control parameter $\mathbf{w}$. The random pressure $P(z, \theta, t; \mathbf{w})$ at the wall of the nozzle is modeled, using cylindrical coordinates, as,

$$P(z, \theta, t; \mathbf{w}) = p_c f(z)\, Z(\theta, t; \mathbf{w})\,. \tag{5}$$

In this equation, p_c is the pressure located at the combustion chamber input of the nozzle and $f(z)$ defines the pressure profile along the nozzle wall. The stochastic process $Z(\theta, t; \mathbf{w})$ is indexed by t in $\mathbb{R}$ and θ in $[0, 2\pi[$, and is parameterized by $\mathbf{w}$. Such a stochastic process is assumed to be almost-surely positive with property $\mathbb{E}\big(Z(\theta, t; \mathbf{w})\big) = 1$ and is defined by

$$Z(\theta, t; \mathbf{w}) = \frac{(1 + G(t; \mathbf{w})b(\theta))^2}{\mathbb{E}\{(1 + G(t; \mathbf{w})b(\theta))^2\}} \quad , \quad b(\theta) = \frac{1}{\mathbb{n} + 1} \sum_{n=0}^{\mathbb{n}} \cos(n\theta), \tag{6}$$

in which $\{G(t; \mathbf{w}), t \in \mathbb{R}\}$ is a Gaussian, second-order, centered, mean-square continuous, stationary stochastic process

[49, 50, 51] whose psd function $\nu \mapsto S_G(2\pi\nu; \mathbf{w})$ is such that the autocorrelation function R_G is written as:

$$R_G(t - t'; \mathbf{w}) = \mathbb{E}\{G(t; \mathbf{w})G(t'; \mathbf{w})\} = \int_{\mathbb{R}} e^{i\omega(t-t')} S_G(\omega; \mathbf{w}) d\omega \,, \tag{7}$$

with $\omega = 2\pi\nu$. Such psd function depends on w and is defined as a concave function with a global maximum in the frequency band. The control parameter $\mathbf{w}$ has two components, w_1 and w_2, such that $\mathbf{w} = (w_1, w_2)$ and they are specified below.

(ii) Prior probability model of $\boldsymbol{W}$. The $\mathbb{R}^2$-valued random control parameter $\mathbf{W} = (W_1, W_2)$ is defined as follows. Control parameter w_1 stands for the time-independent standard deviation σ_G of the random variable $G(t; \mathbf{w})$ for fixed t. Control parameter w_1 is modeled by a random variable W_1 whose mean value is $\underline{w}_1$ and its probability distribution is uniform on the interval $[(1 - \alpha_1)\underline{w}_1 \,,\, (1 + \alpha_1)\underline{w}_1]$ with $\alpha_1 < 1$. Let ν_{peak} be the frequency for which the psd function attains its global maximum. Control parameter w_2 stands for ν_{peak} and is modeled by a uniform random variable W_2 on the interval $[(1 - \alpha_2)\underline{w}_2 \,,\, (1 + \alpha_2)\underline{w}_2]$ with $\alpha_2 < 1$, independent from W_1, with mean value $\underline{w}_2$.

(iii) Prior probability model of $\boldsymbol{U}$. The mean (6x6) elasticity matrix, $[c]$, corresponds to an isotropic elastic medium with given Young modulus and Poisson coefficient. Uncontrolled random parameter $\mathbf{U}$ introduces uncertainty to the Hooke elasticity matrix $[c]$, which yields a random Hooke elasticity matrix, $[\mathbf{C}]$. Uncontrolled random parameter $\mathbf{U}$ corresponds to the 21 entries related to the Cholesky factorization of the random matrix $[\mathbf{G}(\delta)]$ that is defined from the random matrix theory [52, 53] and which yields $[\mathbf{C}]$ such that

$$[\mathbf{C}] = [L_c]^T [\mathbf{G}(\delta)] [L_c] \quad \text{with} \quad [c] = [L_c]^T [L_c] \,, \tag{8}$$

in which δ is a scalar parameter that controls the statistical fluctuations. Note that the probability model of $[\mathbf{G}(\delta)]$ and its random generator can be found in [52].

4. Definition of the training dataset

The parameterized nonlinear uncertain stochastic computational model is used for generating the training dataset. Let us introduce a time sampling $\mathcal{T} = \{t_1, \ldots, t_{N_t}\} \subset T$, in which $t_\alpha = t_0 + (\alpha - 1)\,\delta t$ for $\alpha = \{1, \ldots, N_t\}$ with $\delta t = (t_{N_t} - t_0)/(N_t - 1)$ the sampling time step. The corresponding frequency sampling, that defines set $\mathcal{F}$ is characterized by $N_\nu = N_t$ frequency points such that $\nu_\beta = -0.5\nu_e + (\beta - 1)\delta\nu$, where ν_e is the sampling frequency and $\delta\nu = \nu_e/N_\nu$ the sampling frequency step. The training dataset is constructed by using the prior probability model introduced for random variables $\mathbf{W}$, $\mathbf{U}$ and G. The n_d realizations of $\mathbf{W}$, $\mathbf{U}$ and G are denoted by $(\mathbf{w}^j, \mathbf{u}^j, g^j)$. The corresponding realizations of the time sampled $\mathbb{Y}$ are $\mathbb{y}^j = (\mathbb{Y}(t_1, \mathbf{w}^j), \ldots, \mathbb{Y}(t_{N_t}, \mathbf{w}^j)) \in \mathbb{R}^{N_{\text{o}}}$ with $N_{\text{o}} = \overline{n}_{\mathbb{y}} \times N_t$ (that also depends on $\mathbf{u}^j$ and g^j). The corresponding realization $\mathbf{o}^j$ in $\mathbb{R}^{N_{\text{o}}}$ of random observation vector $\mathbf{O}$ is such that $\mathbf{o}^j = (\mathbb{O}(\nu_1, \mathbf{w}^j), \ldots, \mathbb{O}(\nu_{N_t}, \mathbf{w}^j)))$. The corresponding realization $\mathbf{o}^j_{\text{id}}$ in $\mathbb{R}^{n_{\text{o}}}$ with $n_{\text{o}} = n_{\text{exp}} \times N_\nu < N_{\text{o}}$, of the random identification observation $\mathbf{O}_{\text{id}}$ is deduced from $\mathbf{o}^j$. The training dataset, $\mathcal{D}_{\text{train}}(\mathbf{x})$, is then defined by

$$\mathcal{D}_{\text{train}}(\mathbf{x}) = \{\, \mathbf{x}^j = (\mathbf{o}^j, \mathbf{o}^j_{\text{id}}, \mathbf{w}^j) \,,\; j \in \{1, \ldots, n_d\}\,\} \,, \tag{9}$$

in which $\mathbf{x}^j$ belongs to $\mathbb{R}^{n_x}$ with $n_x = N_{\text{o}} + n_{\text{o}} + n_w$. Such training dataset $\mathcal{D}_{\text{train}}(\mathbf{x})$ is then represented by the $(n_x \times n_d)$ real matrix $[x_d]$ whose columns are constituted of vectors $\mathbf{x}^1, \ldots, \mathbf{x}^{n_d}$. As explained in Section 2, we recall that each realization j of $\mathcal{D}_{\text{train}}$ is obtained from two computational simulations of the corresponding deterministic nonlinear computational model for which the input is constituted of $(\mathbf{w}^j, \mathbf{u}^j, g^j)$. The large nozzle computational model combined with geometrical nonlinearities induces a high computational cost for each realization computation. Consequently, the value of n_d must be limited and remains relatively small.

5. Definition of the target dataset

The target dataset is constructed from N_r given values $\mathbf{w}^r_{\text{targ}} \in C_w$, $r \in \{1, \ldots, N_r\}$ of control parameter $\mathbf{w}$, that correspond to an experimental configuration of the dynamical system. We denote by $\mathcal{W}_{\text{targ}} = \{\mathbf{w}^1_{\text{targ}}, \ldots, \mathbf{w}^{N_r}_{\text{targ}}\}$ the set

of these control-parameter values. For a given control parameter $\mathbf{w}^r_{\text{targ}}$, the target observation vector $\mathbf{o}^r_{\text{targ}} \in \mathbb{R}^{n_o}$ is defined by the family $\{\mathbb{O}_{\text{id}}(\nu; \mathbf{w}^r_{\text{targ}}), \nu \in \mathcal{F}\}$. It is generated from the nonlinear stochastic uncertain computational model for which the uncontrolled parameter $\mathbf{U}$ has been fixed to $\mathbf{U} = \mathbf{u}_{\text{targ}}$. We then denote by $\mathcal{D}_{\text{targ}}(\mathbf{o}_{\text{id}}) = \{\mathbf{o}^1_{\text{targ}}, \ldots, \mathbf{o}^{N_r}_{\text{targ}}\}$ the corresponding target dataset, that is related to an incomplete dataset that will be used in the updating process for constructing a random surrogate predictive model of the uncertain dynamical behavior of the nozzle structure.

6. Updating formulation using probabilistic learning

The objective is to construct a predictive statistical surrogate model for the nozzle, defined by the $\mathbb{R}^{N_o}$-valued random variable $\mathbf{O}_{\text{ud}}$ that represents the probabilistic updating of the $\mathbb{R}^{N_o}$-valued random observation $\mathbf{O}$ defined by Eq. (4). The difficulty of such a problem concerns the cost limitations induced by the high dimension of the parameterized nonlinear stochastic uncertain computational model. This yields a small training dataset which is also characterized by the availability of a partial observation that is localized at the outer radius of the nozzle exit. This also yield a small target dataset that is characterized by a lack of data for which the identification observation has a limited dimension, which can be interpreted by a limited available number of measurement locations. The PLoM under the constraints defined with the target dataset is used for generating independent realizations of the $\mathbb{R}^{N_o}$-valued updated random observation $\mathbf{O}_{\text{ud}}$, which define the learning dataset, $\mathcal{D}_{\text{learn}}(\mathbf{x}_{\text{ud}})$, such that

$$\mathcal{D}_{\text{learn}}(\mathbf{x}_{\text{ud}}) = \left\{\mathbf{x}^\ell_{\text{ud}} = (\mathbf{o}^\ell_{\text{ud}}, \mathbf{o}^\ell_{\text{id,ud}}, \mathbf{w}^\ell), \ell \in \{1, \ldots, N_{\text{ud}}\}\right\} \quad , \tag{10}$$

in which N_{ud} is the number of learned realizations (that is a very large number) and where $\mathbf{x}^\ell_{\text{ud}} \in \mathbb{R}^{n_x}$. From this learned dataset, the conditional probability density function $p_{\mathbf{O}_{\text{ud}}|\mathbf{W}_{\text{ud}}}(\mathbf{o}|\mathbf{w})$ of random variable $\mathbf{O}_{\text{ud}}$ given $\mathbf{W}_{\text{ud}} = \mathbf{w}$ that characterizes the probabilistic surrogate model is computed. The calculation is carried out in two steps. First, the learned dataset $\mathcal{D}_{\text{learn}}(\mathbf{x}_{\text{ud}})$ allows for evaluating the joint pdf $p_{\mathbf{O}_{\text{ud}},\mathbf{W}_{\text{ud}}}(\mathbf{o}; \mathbf{w})$ using the Gaussian Kernel Density Estimation. Secondly, an explicit integration with respect to $\mathbf{o}$ is carried out from the estimated joint pdf in order to evaluate pdf $p_{\mathbf{W}_{\text{ud}}}(\mathbf{w})$. The conditional pdf $p_{\mathbf{O}_{\text{ud}}|\mathbf{W}_{\text{ud}}}(\mathbf{o}|\mathbf{w})$ is then deduced from the relation

$$p_{\mathbf{O}_{\text{ud}},\mathbf{W}_{\text{ud}}}(\mathbf{o}; \mathbf{w}) = p_{\mathbf{O}_{\text{ud}}|\mathbf{W}_{\text{ud}}}(\mathbf{o}|\mathbf{w})\, p_{\mathbf{W}_{\text{ud}}}(\mathbf{w}) \quad . \tag{11}$$

The conditional statistics can be performed independently on each component $k = (i, \beta)$ of $\mathbf{O}_{\text{ud}}$, that corresponds to a given observation number i and to a given frequency ν_β. Let $Z_{i,\beta}(\mathbf{w})$ be the conditional random variable given $\mathbf{W}_{\text{ud}} = \mathbf{w}$, defined by

$$Z_{i,\beta}(\mathbf{w}) = \left(\mathbf{O}_{\text{ud,obs}}(\mathbf{w})\right)_k \quad , \tag{12}$$

We are interested in estimating $p_{\mathbf{Z}_{i,\beta}|\mathbf{W}_{\text{ud}}}(\mathbf{z}|\mathbf{w})$ in order to observe the corresponding conditional confidence region with a given probability level. These conditional confidence regions can be compared to the conditional mean responses of the training and of the target, for a given value of control parameter $\mathbf{w}$.

7. Numerical methodology for constructing the training dataset from the parameterized nonlinear stochastic uncertain computational model

7.1. Modal content analysis of the linear nozzle structure

It is essential to acquire a comprehensive understanding of the modal content exhibited by the nozzle structure. For that, an in-depth analysis is performed in order to identify the optimal frequency domain for which the nonlinear vibrational behavior is complex. In particular, such an analysis allows for choosing (1) the frequency content related to the stochastic excitation and, (2) the frequency band of analysis (given that nonlinear geometric effects induce frequency responses of the nozzle outside the excitation frequency band). For that, we solve the generalized eigenvalue problem for a reference computational model, defined as the associated linear, conservative, homogeneous dynamical system for which the uncontrolled parameter $\mathbf{U}$ is fixed to $\underline{u}$, where $\underline{u}$ is the mean value of $\mathbf{U}$, defined such that $[\mathbf{G}(\delta)] = [I_6]$, and consequently $[\mathbf{C}]$ coincides with isotropic $[c]$ (see Section 3). Section 3. Let $[K(\underline{u})]$ and $[M]$ be the $(n_y \times n_y)$ symmetric positive-definite finite element mass and elastic stiffness matrices. The following generalized

eigenvalue problem is solved in order to obtain the structural modes $\boldsymbol{\varphi}_\alpha$ related to the $n_q \lll n_y$ smallest eigenvalues λ_α such that

$$[K(\underline{u})]\,\boldsymbol{\varphi}_\alpha = \lambda_\alpha [M]\boldsymbol{\varphi}_\alpha \quad , \quad \alpha = \{1, \ldots, n_q\} \quad . \tag{13}$$

In Eq. (13), the elastic structural modes $\boldsymbol{\varphi}_\alpha$ satisfy the orthogonality properties $\boldsymbol{\varphi}_\alpha^T\,[M]\,\boldsymbol{\varphi}_\beta = \delta_{\alpha\beta}$ and $\boldsymbol{\varphi}_\alpha^T\,[K(\underline{u})]\,\boldsymbol{\varphi}_\beta = \lambda_\alpha\,\delta_{\alpha\beta}$, where $\delta_{\alpha\beta}$ denotes the Kronecker symbol that is equal to 1 if $\alpha = \beta$ and 0 otherwise. Since matrices $[K(\underline{u})]$ and $[M]$ are those of an axisymmetric dynamical system, the elastic modes are interpreted in a cylindrical coordinate system, for which the circumferential wave number is $n \in \mathbb{N}$. For each $n > 0$, there is one symmetric and one antisymmetric mode. Such an analysis allows for identifying radial modes ($n = 0$) for which the deformations are purely radial, flexural modes ($n = 1$) corresponding to global bending displacements, and breathing modes ($n \geq 2$) exhibiting local bending deformations [54, 55]. The construction of psd function $\nu \mapsto S_G(2\pi\nu; \mathbf{w})$ of stationary stochastic process $\{G(t; \mathbf{w}), t \in \mathbb{R}\}$ is carefully designed to ensure exciting the breathing modes. The choice of (1) the truncation order $\mathbb{n}$ in the series $b(\theta)$ defined by Eq. (6) and of (2) the sampling frequency ν_e are directly related to the modal content of the nozzle structure.

7.2. Nonlinear computational solver

Each point of the training dataset is obtained by solving successively two initial value problems corresponding to a given large-dimension deterministic nonlinear differential equation. An implicit unconditionally stable integration scheme is chosen as the Newmark method with an averaging acceleration scheme [56]. With such an integration scheme, for a given realization $(\mathbf{u}^j, \mathbf{w}^j)$ of $(\mathbf{U}, \mathbf{W})$ and for a given sampling time t_α, we then have to solve the following set of nonlinear coupled equations such that, for $\alpha = 1, \ldots, N_t$,

$$[K^{\text{eff}}(\mathbf{u}^j)]\,\mathbf{Y}(t_\alpha; \mathbf{w}^j) + \mathbf{F}^{\text{NL}}(\mathbf{Y}(t_\alpha; \mathbf{w}^j), \mathbf{u}^j) = \mathbf{f}^{\text{eff}}(t_\alpha; \mathbf{w}^j, \mathbf{u}^j). \tag{14}$$

In Eq. (14), the matrix $[K^{\text{eff}}(\mathbf{u}^j)]$ is the reduced effective stiffness matrix that is time independent. Note that $[K^{\text{eff}}(\mathbf{u}^j)]$ is positive definite. The vector $\mathbf{f}^{\text{eff}}$ models the effective external load. The nonlinear algorithm can switch from Newton-Raphson algorithm to an adapted [57] arc-length algorithm [58, 59, 60, 61, 62]. For each time step, the tangent matrix is constructed and an iteration loop is introduced between two consecutive time steps for obtaining the equilibrium.

8. Finite element computational model of the nozzle

Let $(O, \mathbf{e}_X, \mathbf{e}_Y, \mathbf{e}_Z)$ be a Cartesian reference coordinate system. The three-dimensional nozzle geometry is generated through axisymmetry around the z-axis from a given generating line $\ell(z)$ that describes a bell-shape nozzle design [63] and whose dimensionless representation is depicted in Figure 3. The height H of the nozzle and the external diameter D_e located at the exit of the nozzle are such that $H/D_e = 1.613$. Its thickness t is assumed to be constant with $t/D_e = 0.015$.

The finite element computational model that is represented in Figure 2 consists of a mesh made up of 57 792 hexahedral solid finite elements with 8 nodes each, resulting in a total of 73 030 nodes and $n_{\text{dof}} = 216\,720$ degrees of freedom. A fixed boundary condition is applied at the entry of the combustion chamber. The computational characteristics described according to the radial (r), orthoradial (θ), and z-axis directions, are summarized in Table 1. It should be noted that the slenderness ratio between the orthoradial and radial dimensions of a finite element is between 1 and 5.04 in order to ensure a good computational accuracy. The nominal material properties of the nozzle structure correspond to a homogeneous isotropic elastic material that represents a homogenized ceramic with Young modulus 170 GPa, Poisson ratio 0.28, and mass density $2300\,\text{Kg} \times \text{m}^{-3}$.

	r	θ	z	Total
number of nodes	5	168	87	73 080
number of finite elements	4	168	86	57 792

Table 1: Finite element model parameters

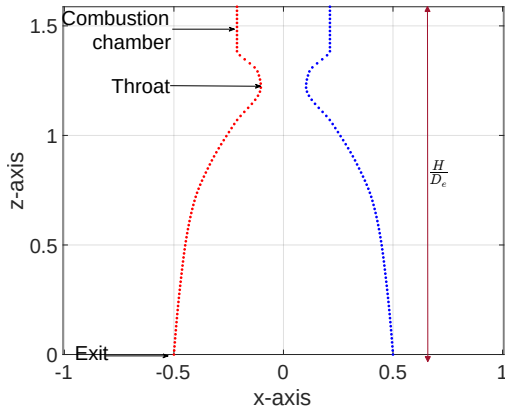

Figure 3: Generating line of the nozzle

9. Modal analysis of the nominal linear nozzle structure

Figure 4 displays the graph of the natural frequencies ν_α as a function of circumferential wave number n, displaying mode families. Such a graph allows for considering a frequency band of analysis $\mathbb{B} = [0\,,\,1500]$ Hz that contains 24 structural modes for which $n \leq 6$. Note that such a choice has to be consistent with the external load modeling. Figure 5 displays $3D$ and $2D$ representations of the first eight structural modes. It is interesting to underline that the

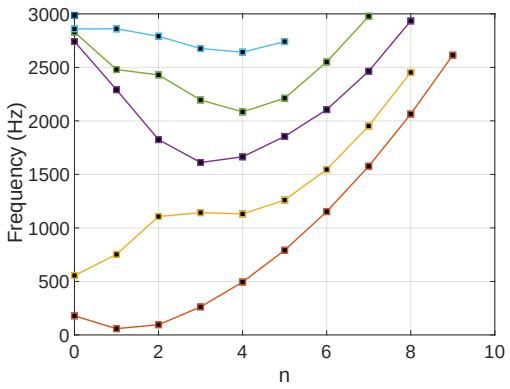

Figure 4: Natural frequencies versus n.

first frequencies are $\nu_1 = 58.55$ Hz, $\nu_2 = 95.61$ Hz, and $\nu_3 = 178.42$ Hz. The fundamental structural mode is a flexural mode related to $n = 1$ that displays a global bending motion of the structure. The second structural mode corresponds to a $n = 2$ breathing mode and the third one is a $n = 0$ axisymmetric mode. Such an analysis shows that the excitation frequency band is centered around ν_2.

10. Stochastic external load

10.1. Description of the pressure profile

The pressure profile $p_c f(z)$ follows the model proposed in [63, 64]. There are three pressure parameters that characterize the nozzle. The pressure at the entry of the combustion chamber is $p_c = 2.413 \times 10^6\,\mathrm{N} \times \mathrm{m}^{-2}$ [64]. The pressure at the nozzle exit is the ambient pressure $p_e = 1.01325 \times 10^5\,\mathrm{N} \times \mathrm{m}^{-2}$. The pressure at the nozzle throat is $p_t = 1.3682 \times 10^6\,\mathrm{N} \times \mathrm{m}^{-2}$ and corresponds to a Mach number $M_t = 1$. The normalized pressure profile along the z-axis is shown in Figure 6 and is constructed as follows. The pressure profile within the throat region is determined through fluid calculations [64] and shown in Figure 7. Considering that there are only 4 nodes along the z-axis within

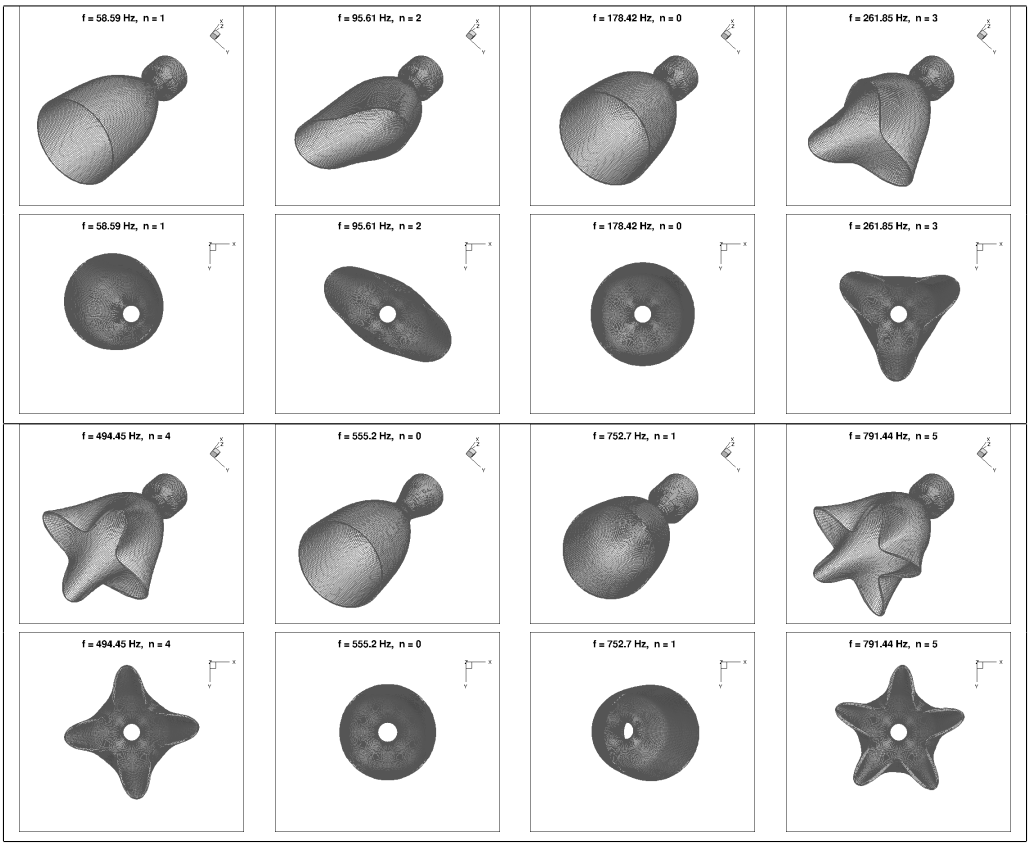

Figure 5: $3D$ and $2D$ representations of the first 8 structural modes

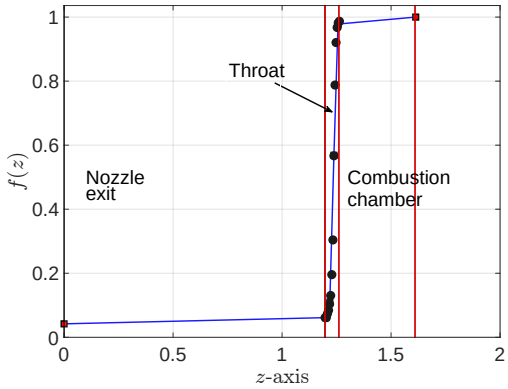

Figure 6: Graph $z \mapsto f(z)$ of the normalized pressure profile. Vertical lines delimit the combustion chamber, the throat, and the nozzle exit parts.

the finite element model of the nozzle throat, while there are 14 pressure values available, a straightforward linear interpolation is performed for obtaining pressure values at the internal nodes of the finite element model for the throat. In the combustion chamber, the pressure profile is linearly interpolated along z with respect to p_c and to the pressure at the beginning of the nozzle throat, while in the nozzle exit, it is linearly interpolated along z with respect to the pressure at the end of the nozzle throat and to the ambient pressure p_e.

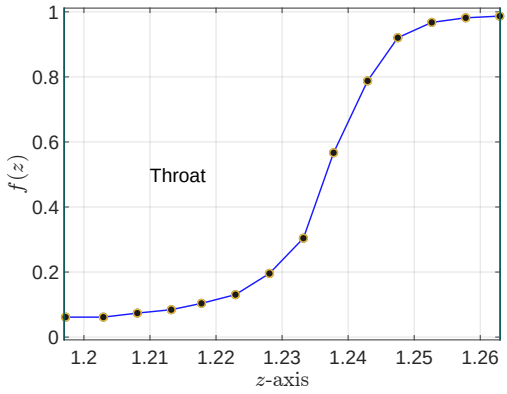

Figure 7: Zoom of graph $z \mapsto f(z)$ in the nozzle throat area.

10.2. Description of the psd function S_G

In Eq. (6), the algebraic model of the psd function $S_G(2\pi\nu)$ is an adaptation of the one proposed in [65], and depends on two parameters σ_G^2 that is the power of the stationary stochastic process G and ν_{peak}, which is the frequency for which the psd function is maximal. This algebraic model is written as

$$S_G(2\pi\nu) = \frac{\sigma_G^2}{\overline{\sigma}^2}\,\overline{S}(2\pi\nu) \quad , \quad \nu \in \mathbb{R} \quad , \tag{15}$$

in which $\sigma_G^2 = 2\int_{\mathbb{R}^+} S_G(2\pi\nu)\,d(2\pi\nu)$. Similarly, $\overline{\sigma}^2 = 2\int_{\mathbb{R}^+} \overline{S}(2\pi\nu)\,d(2\pi\nu)$, where the function $\overline{S}(2\pi\nu)$ is defined by $\overline{S}(2\pi\nu) = 10^{\mathbb{p}(\aleph)/10}$, in which $\aleph = \log_{10}(\nu/\nu_{\text{peak}})$. Function $\mathbb{p}(\aleph)$ depends on parameter ν_{peak} and is defined by $\mathbb{p}(\aleph) = \alpha\aleph^2 + \beta\aleph + \gamma$ for $\aleph \in [\aleph_{\min}, \aleph_{\max}]$. The bounds are such that $\aleph_{\max} = \log_{10}(\nu_{\max}/\nu_{\text{peak}})$ and $\aleph_{\min} = -\aleph_{\max}$ implying that $\nu_{\min} = \nu_{\text{peak}}^2/\nu_{\max}$. Excitation frequency band $\mathbb{B}_e$ is then defined by $\mathbb{B}_e = [\nu_{\min}\,,\,\nu_{\max}]$. The parameters α, β and γ are derived from the following conditions: $\mathbb{p}(\aleph_{\min}) = \mathbb{p}(\aleph_{\max}) = p_{\min} < 0$, and $\mathbb{p}(0) = 1$. This latter condition corresponds to a normalization choice yielding $\mathbb{p}(\aleph) = (p_{\min} - 1)(\aleph/\aleph_{\max})^2 + 1$. The numerical values are the following: $\nu_{\max} = 1200\,\text{Hz}$, $\nu_{\text{peak}} = 100\,\text{Hz}$, which is very close to the eigenfrequency ν_2 corresponding to a breathing mode with circumferential wave number $n = 2$, $\nu_{\min} = 8.33\,\text{Hz}$, and $\mathbb{B}_e = [8.33\,,\,1200]\,\text{Hz}$. Since the frequency band of analysis $\mathbb{B}$ only contains structural modes with circumferential wave number lower than 6, the series $b(\theta)$ is limited to $\mathbb{n} = 6$.

10.3. Time and frequency samplings for computing the stochastic nonlinear response

Time t_0 that corresponds to the beginning of the stationary response of the nonlinear dynamical system is identified as follows. The damping model used in the nonlinear computational model corresponds to a modal damping model for which the critical damping rate ξ_α related to eigenfrequency ν_α is set to $\xi_\alpha = 0.02$. Then the duration time $|T_0| = t_0 - 0 = 0.998\,\text{s}$ is chosen to be consistent with the relaxation time of the dynamical system. Then the sampling time step δt is chosen as $\delta t = 20\,\text{ms}$ yielding $N_t = 5\,000$ time points such that $t_\alpha = t_0 + (\alpha - 1)\delta t\,,\ \alpha \in \{1, \ldots, N_t\}$. As a consequence, the sampling frequency is $\nu_e = 3\,000\,\text{Hz}$. There are $N_\nu = 5\,000$ sampling frequency points with sampling frequency step $\delta\nu = 0.6\,\text{Hz}$. For $\sigma_G = 0.4$ and $\nu_{\text{peak}} = 100\,\text{Hz}$, Figure 8 displays the graph of the algebraic psd function $\nu \mapsto S_G(2\pi\nu)$ defined by Eq. (15), and the graph of its estimation computed from $n_d = 400$ realizations of the stationary stochastic process G.

11. Specifying the prior probabilistic model, the stochastic solver, and the target dataset

As explained in Section 3-(ii), the two control parameters are $w_1 = \sigma_G$ and $w_2 = \nu_{\text{peak}}$, which are modeled by random variables W_1 and W_2.

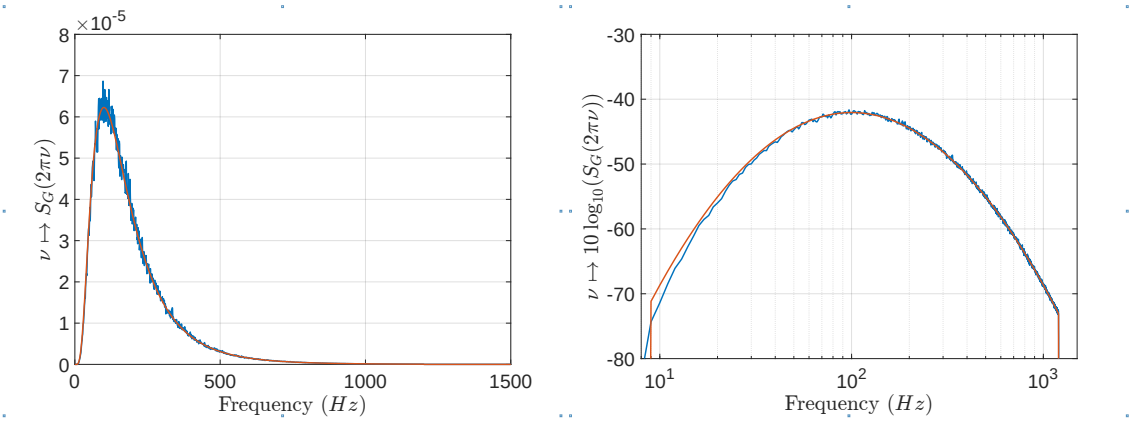

(a) Linear scale

(b) Log-log scale

Figure 8: Graph of $\nu \mapsto S_G(2\pi\nu)$ for $\sigma_G = 0.4$ and $\nu_{\text{peak}} = 100\,\text{Hz}$ (algebraic (red line), estimate (blue line)).

11.1. Numerical values for the nominal computational model

The nominal computational model of the nozzle corresponds to a parameterized model with the mean value $\underline{w}_1 = 0.4$ of W_1, the mean value $\underline{w}_2 = 100\,\text{Hz}$ of W_2, and the mean value $\underline{\mathbf{u}}$ of random vector $\mathbf{U}$. This random vector $\mathbf{U}$ is related to the random matrix $[\mathbf{C}]$, defined by Eq.(8). For these nominal values $\underline{\mathbf{w}}$ and $\underline{u}$, the maximum of the deterministic nonlinear dynamical response in displacement is of the same order than the nozzle thickness, that ensures the presence of geometrically nonlinear effects.

11.2. Numerical values for the hyperparameters of the prior probabilistic model

The values of the hyperparameters defined in Section 3-(ii) are $\alpha_1 = \alpha_2 = 0.1$.The admissible set $C_w \subset \mathbb{R}^2$ of $\mathbf{W}$ is defined by $C_w = \{[0.36, 0.44] \times [90, 110]\}$. The hyperparameter δ defined in Section 3-(iii) is chosen as $\delta = 0.2$.

11.3. Stochastic solver

As explained in Section 4, the training dataset is constructed by using the Monte Carlo numerical simulation method. Due to the limitation of the computational resources, $n_d = 400$ realizations of the training set are considered. The realizations $\mathbf{w}^j$ and $\mathbf{u}^j$ are generated using the prior probability model of $\mathbf{W}$ and $\mathbf{U}$. The realizations g^j representing the time discretization of the stationary stochastic process G are generated using the Shinozuka algorithm [66, 67]. For a given realization $(\mathbf{w}^j, \mathbf{u}^j, g^j)$, the parameterized stochastic computational model is used to get a realization of the stochastic response $\mathbf{y}^j(t) = \mathbf{Y}(t; \mathbf{w}^j, \mathbf{u}^j, g^j)$ and then deducing the realizations of the observations. The realization $\mathbf{o}_d^j$ is the corresponding realization of $\mathbf{O}$. For a given frequency, it corresponds to the $\overline{n}_y = 168$ normal bending displacements located at the outer radius of the nozzle. It has dimension $N_{\text{o}} = 168 \times 5000 = 840\,000$. The realization $\mathbf{o}_{\text{id},d}^j$ is the corresponding realization of $\mathbf{O}_{\text{id}}$ of the identification observation, which is related to a subset of $n_{\text{exp}} = 8$ partial observations. It has dimension $n_{\text{o}} = 8 \times 5000 = 40\,000$. It results that the training dataset can be stored in matrix $[\mathbb{x}^d]$ with dimensions $(880002, 400)$. Figure 9 displays an unscaled representation of the nodes located at the nozzle exit in order to visualize the location of the identification observation nodes and of a distinct group of validation observation nodes.

11.4. Description of the target dataset

The target dataset $\mathcal{D}_{\text{targ}}$ is constructed as independent realizations of the stochastic nonlinear computational model, for which $\delta = 0$ (no uncertainties) and the value of $[c]$ is modified as $\alpha_c[c]$ with $\alpha_c = 1.2$. The $N_r = 40$ values of the control parameter $\mathbf{w}_{\text{targ}}$ are the realizations of a uniform probability distribution whose support is C_W.

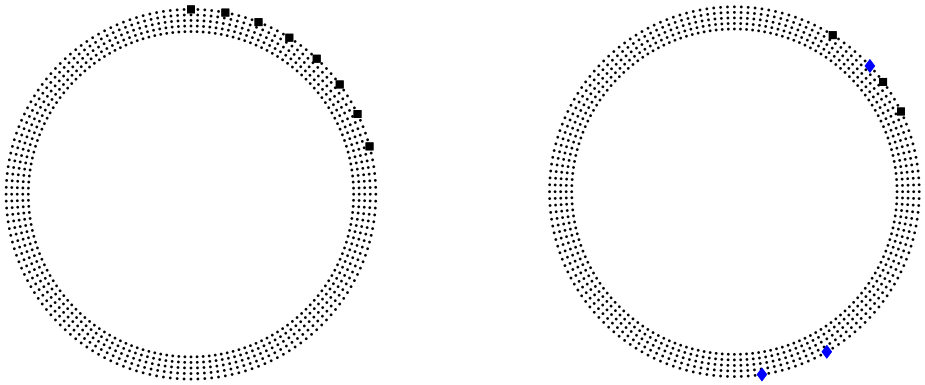

(a) Training and target. (b) Learning post-processing.

Figure 9: Location of identification observations (black squares) and validation observations (blue diamonds).

12. Parameter values and convergence analysis of PLoM algorithm

We use the notations introduced in Appendix Appendix A.

(i) Values of the general parameters. The dimension of $\mathbf{Q} = (\mathbf{O}, \mathbf{O}_{\text{id}})$ is $n_q = N_{\text{o}} + n_{\text{o}} = 840\,000 + 40\,000 = 880\,000$ and the dimension of $\mathbf{X} = (\mathbf{Q}, \mathbf{W})$ is $n_x = n_q + n_w = 880\,000 + 2 = 880\,002$. The number of points in the training dataset $\mathcal{D}_{\text{train}}$ is $n_d = 400$.

(ii) Reduced representation and diffusion-maps basis. Figure 10a displays the graph of function $\nu_p \mapsto \text{err}_{\mathbf{X}}(\nu_p)$ defined by Eq. (A.2). The chosen tolerance is $\varepsilon_{\text{PCA}} = 0.07$, resulting in $\nu_p = 307$ and an associated error of $\text{err}_{\mathbf{X}}(307) = 6.2 \times 10^{-2}$. It should be noted that the slow decrease of the PCA error function is mainly due to the presence of numerous independent random variables required to construct the model of the stationary stochastic process, which models the stochastic load vector (see Section 3-(i)). It should also be noted that the purpose of the PCA in PLoM is the construction of a random vector $\mathbf{H}$ with zero mean and unit covariance matrix (see Appendix Appendix A-(iv). A relatively large value of ν_p does not affect the PLoM method.

Concerning the computation of the diffusion-maps basis introduced in Appendix Appendix A-(vi), the optimal smoothing parameter ε_{DM} is determined as $\varepsilon_{\text{opt}} = 674$, corresponding to the optimal value $m_{\text{opt}} = 308$ for the parameter m. The graph in Figure 10b presents the function $\alpha \mapsto \lambda_\alpha$, representing the eigenvalues of the transition matrix $[\mathbb{P}]$.

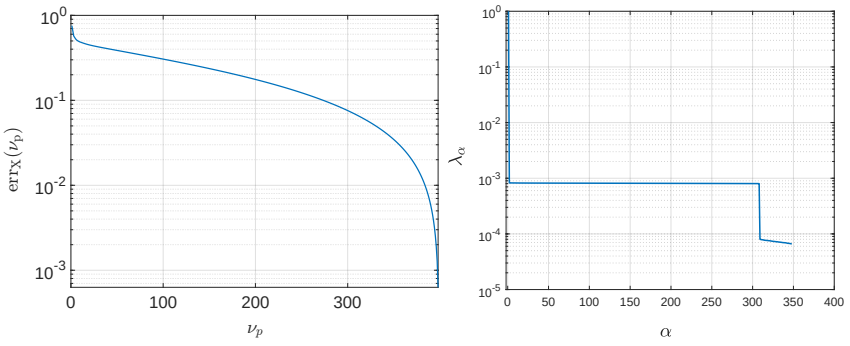

(a) Graph of $\nu_p \mapsto \text{err}_{\mathbf{X}}(\nu_p)$ (b) Graph of $\alpha \mapsto \lambda_\alpha$

Figure 10: Convergence of PCA (a). Eigenvalues of the transition matrix $[\mathbb{P}]$ for the diffusion-maps basis (b).

(iii) Parameter values for generating the learned realizations under constraint. The learned realizations are generated as explained in Appendix Appendix A-(xii), incorporating the vector-valued constraint outlined in Eq. (A.6),

for which $N_r = 40$ (number of targets). The free parameter f_0, defined in Appendix Appendix A-(viii)-(e), is set to $f_0 = 4$, and the integration step Δr of the Störmer-Verlet scheme is chosen as $\Delta_r = 0.218$. Let $\{[\mathcal{Z}_{\text{ud}}(r)], r \in [0, R]\}$ be the stochastic solution of the reduced-order ISDE defined in Appendix Appendix A-(viii), in which Eq. (A.3) is replaced by Eq. (A.9), as explained in Appendix Appendix A-(xii). Each realization $[z_{\text{ud}}^{\ell}]$ represents the ℓth realization of $[\mathcal{Z}_{\text{ud}}(R)]$ for $R = 30 \times \Delta r$. Due to the damping controlled by $f_0 = 4$, R is a final value of integration parameter r of the reduced-order ISDE, at which the stationary response is attained. We have chosen $n_{\text{MC}} = 125$, resulting in $N_{\text{ud}} = n_{\text{MC}} \times n_d = 50\,000$.

(iv) Convergence of the sequence of vector-valued Lagrange multipliers in the KLDMP. The relaxation parameter $\alpha_{\text{relax}}(i)$ (refer to Appendix A-(xiii)) is defined by $\beta_1 = 0.001, i_2 = 20$, and $\beta_2 = 0.3$. The convergence behavior of the iterative algorithm, presented in Appendix Appendix A-(xiii), accounting for the imposed constraints is investigated concerning the iteration number i. This analysis is conducted by examining the graph of the error function $i \mapsto \text{err}(i)$ defined by Eq. (A.8) (refer to Figure 11a) and the graph of the function $i \mapsto \|\boldsymbol{\lambda}^i\|$ (refer to Figure 11b). A very good convergence is observed, with $\text{err}(80) = 5 \times 10^{-4}$.

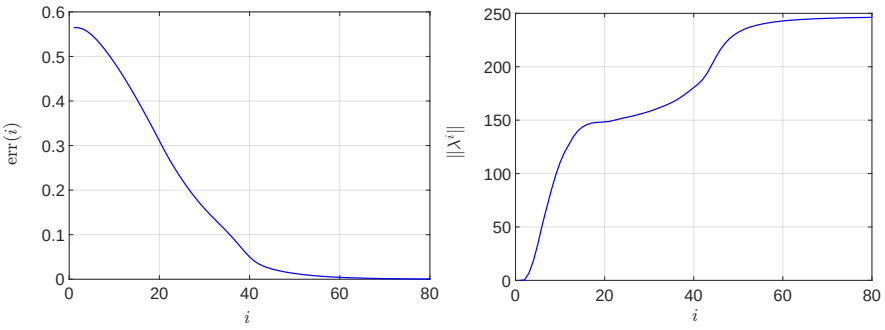

(a) Graph of $i \mapsto \text{err}(i)$ (b) Graph of $i \mapsto \|\boldsymbol{\lambda}^i\|$

Figure 11: Convergence analysis of the iterative algorithm in PLoM with constraints versus iteration number i.

(v) Illustration of the learned pdf of components of $\boldsymbol{H}_{\text{ud}}$ and the clouds of the learned points. Figure 12 depicts the pdf of components 1 and 30 of $\mathbf{H}$ estimated using the training dataset, and the corresponding pdf of $\mathbf{H}_{\text{ud}}$ estimated with the learned dataset under constraint. Figure 13 displays the point cloud of components 7, 13, and 30 of $\mathbf{H}$ estimated with the training dataset, and the corresponding point cloud of $\mathbf{H}_{\text{ud}}$ estimated with the learned dataset under constraint. These results serve to illustrate the shift in the learned probability measure induced by the constraints, while preserving the concentration of the learned probability measure.

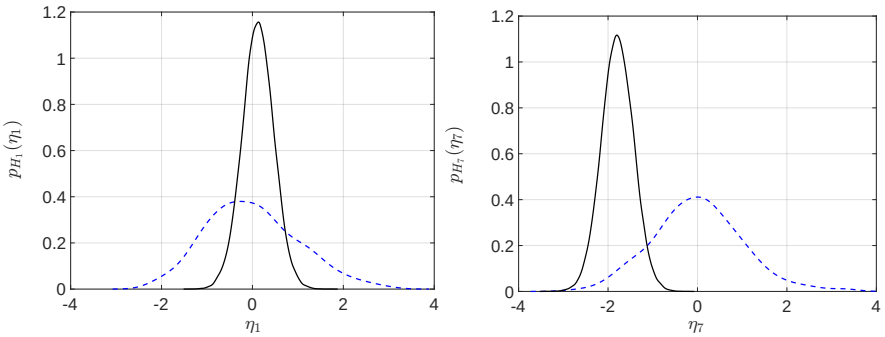

(a) PDF $\eta_1 \mapsto p_{H_1}(\eta_1)$ (b) PDF $\eta_{30} \mapsto p_{H_{30}}(\eta_{30})$

Figure 12: pdfs of components 1 and 30 for $\mathbf{H}$ (dashed line) and for $\mathbf{H}_{\text{ud}}$ (solid line).

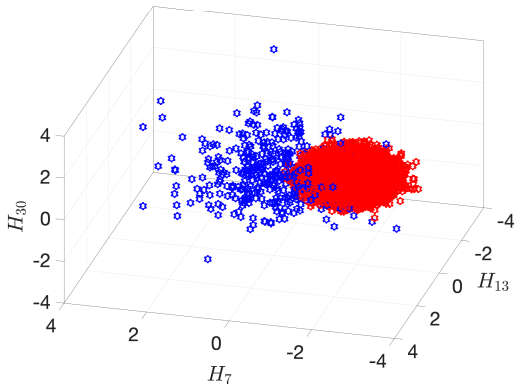

Figure 13: Points cloud of components 7, 13, and 30 for $\mathbf{H}$ (sparse blue) and for $\mathbf{H}_{\text{ud}}$ (concentrated red).

13. Learning results and validation

Figures 14 to 16 are related to a selection of three identification observations whereas Figures 17 to 19 are related to a selection of three validation observations. Each one of Figures 14 to 19 are composed of (a) the mean response of the training dataset – which is a nonlinear response – and of its linear counterpart, (b) the mean response of the training dataset and of the target, (c) the mean response of the learning dataset and of the target, (d) the mean response of the training dataset and of the target, as well as the conditional confidence region given $w_0 = (1, 1)$ of the learning dataset, with a 95% probability level.
– In each Figure (a), significant nonlinear effects are put into evidence, which translate into a shifting of the resonance peaks as well as into a decrease of their magnitude induced by the spread of the response energy throughout the excitation band.
– In each Figure (b), it can be seen that the mean response of the training dataset does not match the mean response of the target. In particular, the second and third nonlinear resonance peaks are shifted.
– Figures (c) show that the learning under constraint of the target captures the mean statistics. Note that the mean responses are not necessarily supposed to coincide, because the system is under-observed for defining the identification constraints and is based on the use of a limited target dataset.
– Figures (d) allow for exhibiting three features of the learning process under constraints. First, the mean target is well centered in the confidence region. Second, the peaks of the confidence-region envelopes coincide well with those of the mean target response. Finally, the width of the confidence region, which is induced by uncertain uncontrolled parameters and by the statistical fluctuations of the stochastic excitation, is not too large.

It should be noted that, for a fixed value of the vector-valued control parameter, the frequency responses conditioned by this control parameter, in the presence of uncontrolled uncertainties, are not the Fourier transforms of deterministic time responses, but that of stationary stochastic processes due to the stationary random excitation of the dynamical system. These frequency responses are therefore similar to a conditional power spectral density function whose estimator is similar to that given by the periodogram method. The intensity of the very small fluctuations that appear in the mean functions and in the envelopes of the confidence regions of these conditional power spectral density functions can be decreased by increasing the value of N_{ud}.

The detailed analysis presented above, concerning figures (a) to (d) for identification and validation observations, serves as validation for the proposed methodology. Further validation could also be provided based on the definition of numerical indicators for statistical errors.

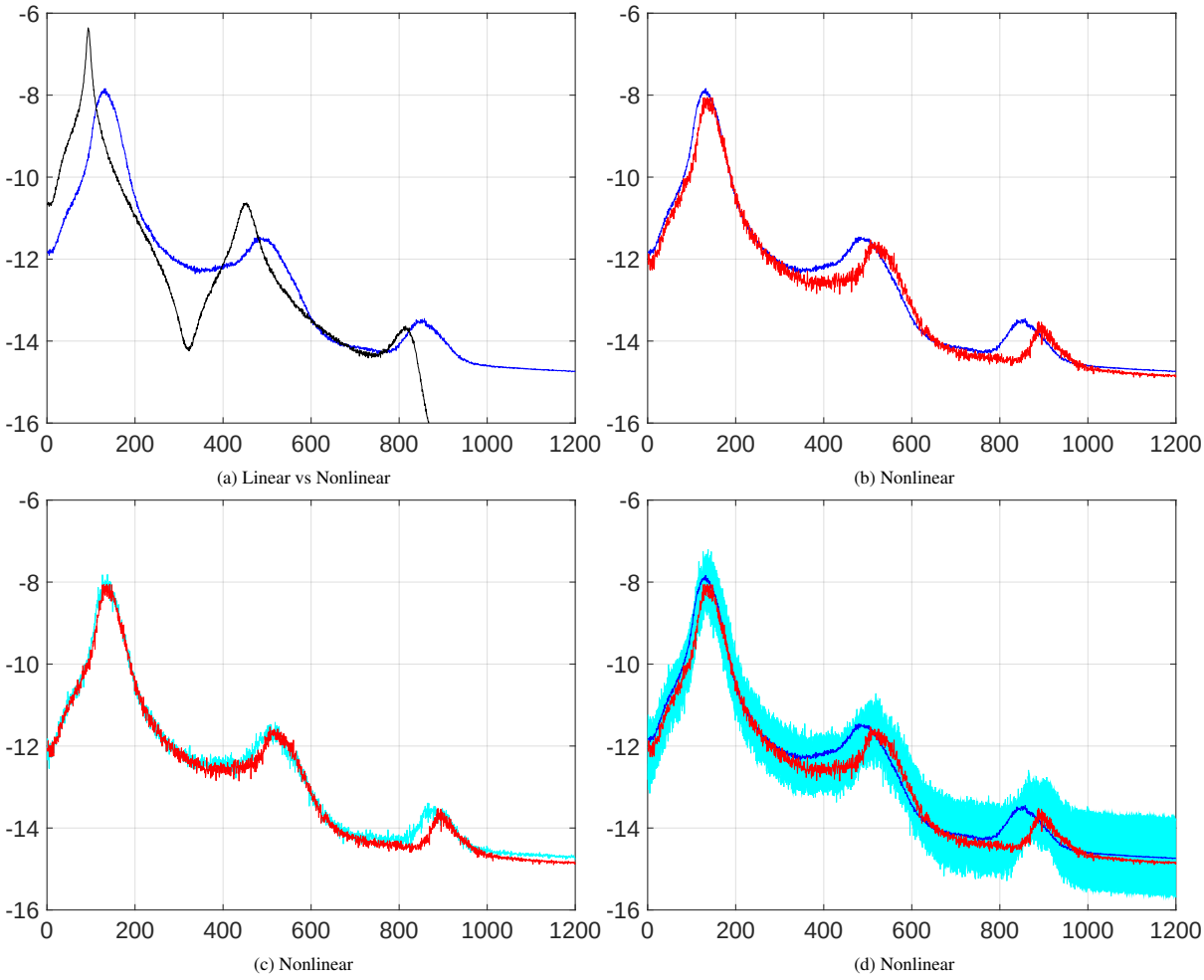

(a) Linear vs Nonlinear

(b) Nonlinear

(c) Nonlinear

(d) Nonlinear

Figure 14: Identification observation 1 – Mean response of the training set (blue line), of the linear counterpart of the training set (black line), of the target set (red line), and of the learning set (cyan line), and confidence region of the learning set (cyan area).

14. Conclusion

We have presented a methodology for the updating of a high dimensional computational model (HDM) corresponding to a nonlinear uncertain dynamical system that is subjected to a stochastic excitation and that is under-observed. The high computational cost resulting from the numerical evaluation of a single realization of the HDM is directly attributed to the presence of uncertain parameters, of global geometric nonlinearities, and of the stochastic nature of the external force. This leads to a small training dataset. The updating is performed under the constraint of a target dataset that is also of small dimension. In addition, there is a partial observability in the dynamical system, which induces incomplete data. For solving this challenging problem, we have presented the construction of a statistical surrogate model that maps the control parameters to the observations. We have presented a detailed and complete analysis of the updating of the nonlinear stochastic dynamics of a nozzle under stochastic excitation and uncertainties. For that, we have applied with success the Probabilistic Learning on Manifolds (PLoM) under constraints. Apart from capturing the geometrically nonlinear effects combined to uncertainty propagation in the under-observed system, the conditional mean statistics of the learning regarding the target dataset are improved compared to its training counterpart. In addition, the conditional confidence region of the learning dataset demonstrates its ability to capture the target characteristics corresponding to either observed output variables (included in the learning optimization process) or unobserved output variables.

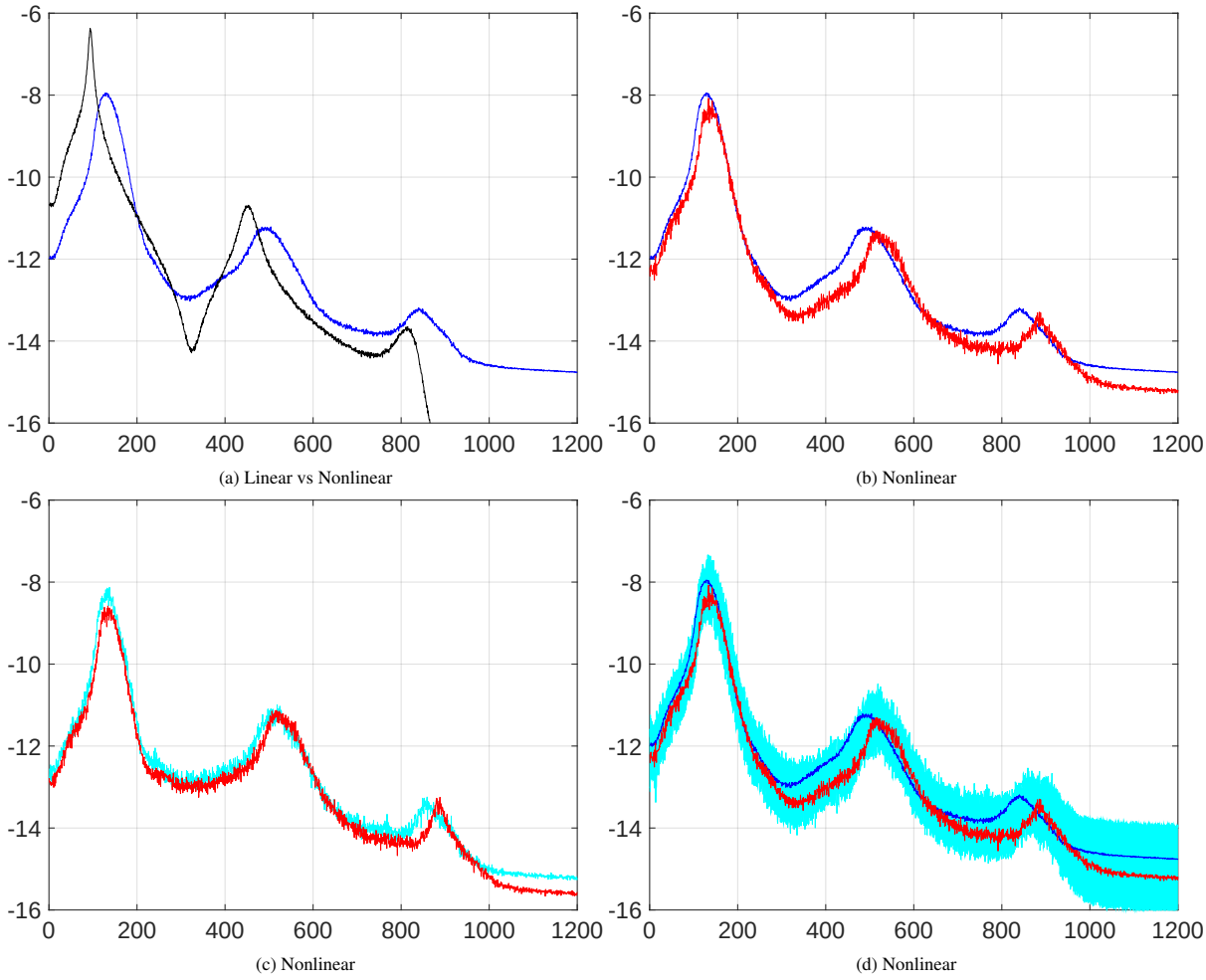

(a) Linear vs Nonlinear

(b) Nonlinear

(c) Nonlinear

(d) Nonlinear

Figure 15: Identification observation 2 (see legend Fig. 14).

Appendix A. Overview of the probabilistic learning on manifolds (PLoM) algorithm and its parameterization

We present the Probabilistic Learning on Manifolds (PLoM) algorithm, detailed in [68], for constrained learning cases. The foundational PLoM approach is outlined in [32, 38, 69], with extensions discussed in [39] for constraints based on statistical moments and [68] for constraints defined by target realizations. Both extensions use the Kullback-Leibler divergence, and the latter employs a weak formulation of the Fourier transform of probability measures. In this Appendix, we focus on the PLoM algorithm for learning under constraints defined by given target realizations. The algorithm starts with a training dataset $\mathcal{D}_{\text{train}}$, comprising a limited number n_d of points generated from a stochastic manifold associated with a $\mathbb{R}^{n_x}$-valued random variable $\mathbf{X} = (\mathbf{Q}, \mathbf{W})$. Here, $\mathbf{Q}$ and $\mathbf{W}$ are $\mathbb{R}^{n_q}$-valued and $\mathbb{R}^{n_w}$-valued random variables, respectively, with $n_x = n_q + n_w$. The support of the probability measure of $\mathbf{W}$ is $C_w \subset \mathbb{R}^{n_w}$. An additional $\mathbb{R}^{n_u}$-valued random variable $\mathbf{U}$ is considered as an uncontrolled parameter. The mapping $\mathbf{f}$ expresses $\mathbf{Q} = \mathbf{f}(\mathbf{U}, \mathbf{W})$, and the joint probability distribution $P_{\mathbf{W},\mathbf{U}}(d\mathbf{w}, d\mathbf{u})$ is assumed known. In constrained learning, the focus is on the quantity of interest $\mathbf{Q} = (\mathbf{O}, \mathbf{O}_{\text{id}})$, where $\mathbf{O}$ and $\mathbf{O}_{\text{id}}$ are $\mathbb{R}^{N_o}$-valued and $\mathbb{R}^{n_o}$-valued random vectors, respectively, with $n_o \ll N_o$ and $n_q = N_o + n_o$. Constraints are applied to $\mathbf{o}_{\text{id}}$. The PLoM under constraint method generates a learned dataset $\mathcal{D}_{\text{learn}}$ for $\mathbf{X}_{\text{ud}}$, comprising $N_{\text{ud}} \gg n_d$ points using a diffusion-maps basis.

(i) Small target dataset $\mathcal{D}_{\text{targ}}(\mathbf{o}_{\text{id}})$. Relatively to $\mathbf{O}_{\text{id}}$, a deterministic target dataset $\mathcal{D}_{\text{targ}}(\mathbf{o}_{\text{id}}) = \{\mathbf{o}^1_{\text{targ}}, \ldots, \mathbf{o}^{N_r}_{\text{targ}}\}$ is given, in which N_r is small. For each r in $\{1, \ldots, N_r\}$, the vector $\mathbf{o}^r_{\text{targ}} \in \mathbb{R}^{n_o}$ corresponds to a "measurement" performed on the dynamical system for a given value $\mathbf{w}^r_{\text{targ}} \in C_w$ of the control parameter $\mathbf{w}$ belonging to $\mathcal{W}_{\text{targ}} = \{\mathbf{w}^1_{\text{targ}}, \ldots, \mathbf{w}^{N_r}_{\text{targ}}\}$.

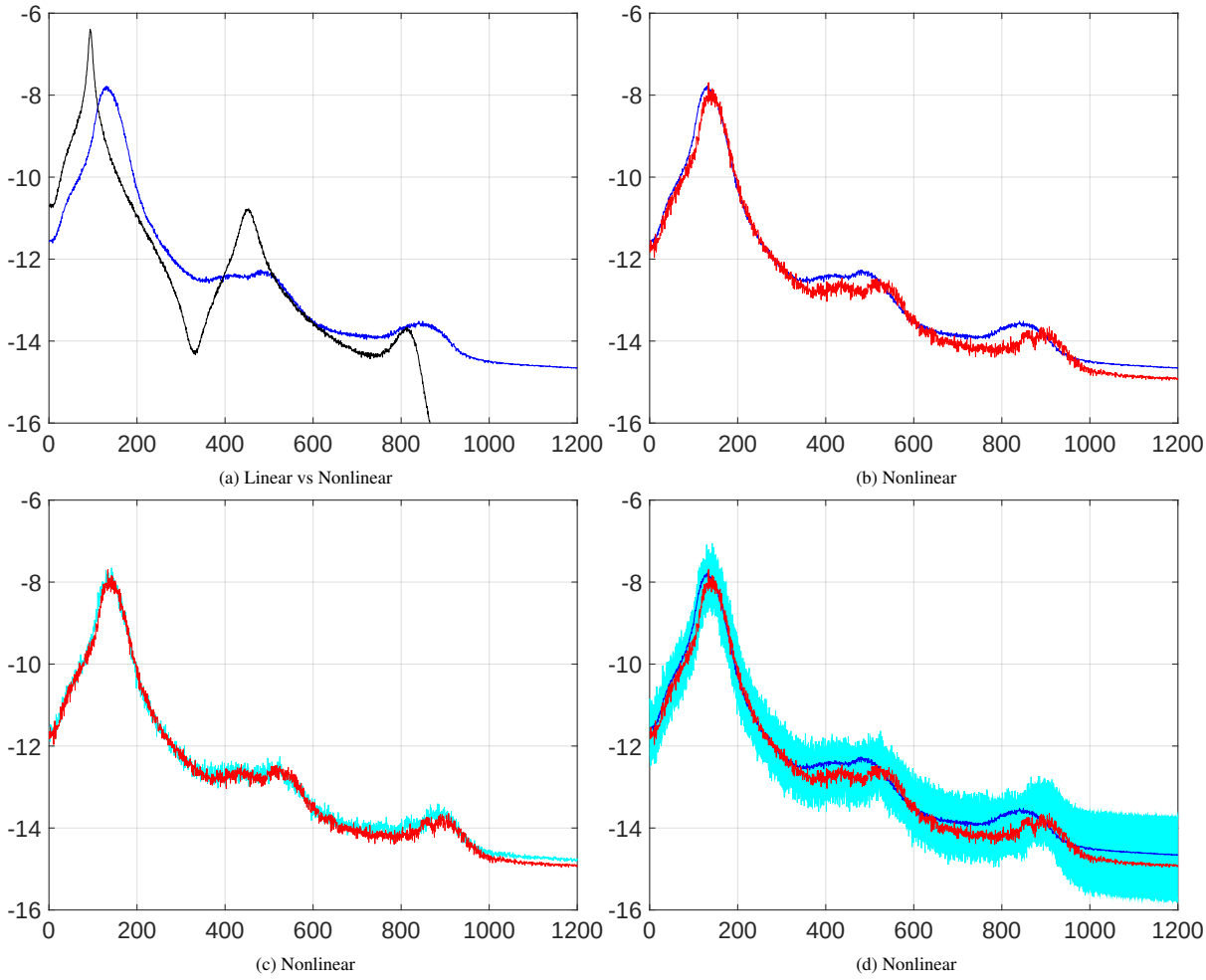

(a) Linear vs Nonlinear

(b) Nonlinear

(c) Nonlinear

(d) Nonlinear

Figure 16: Identification observation 3 (see legend Fig. 14)

(ii) Small training dataset $\mathcal{D}_{\text{train}}(\mathbf{x})$. For all $j \in \{1, \ldots, n_d\}$, we define $\mathbf{x}^j = (\mathbf{o}^j, \mathbf{o}^j_{\text{id}}, \mathbf{w}^j) \in \mathbb{R}^{n_x}$ with $n_x = N_{\text{o}} + n_{\text{o}} + n_w$. The training dataset relative to the small number n_d of points $\mathbf{x}^j$ is $\mathcal{D}_{\text{train}}(\mathbf{x}) = \{\mathbf{x}^1, \ldots, \mathbf{x}^{n_d}\}$ and is represented by the matrix $[x_d] = [\mathbf{x}^1 \ldots \mathbf{x}^{n_d}] \in \mathbb{M}_{n_x, n_d}$.
(iii) Significant learning challenge. The primary difficulty to the learning process arises from the limited number of points in both the training and target datasets, exacerbated by incomplete data resulting from partial observability.
(iv) Reduced representation of $\boldsymbol{X}$ *using PCA and convergence criterion*. Let $[\mathbf{X}] = [\mathbf{X}^1, \ldots, \mathbf{X}^{n_d}]$ be the random matrix with values in $\mathbb{M}_{n_x, n_d}$, where its columns are n_d independent copies of random vector $\mathbf{X}$ for which $[x_d]$ is a realization. Utilizing Principal Component Analysis (PCA) of $\mathbf{X}$, random matrix $[\mathbf{X}]$ is written as,

$$[\mathbf{X}] = [\underline{x}] + [\varphi]\,[\mu]^{1/2}\,[\mathbf{H}]\,, \tag{A.1}$$

where $[\mathbf{H}] = [\mathbf{H}^1, \ldots, \mathbf{H}^{n_d}]$ is a $\mathbb{M}_{\nu_p, n_d}$-valued random matrix ($\nu_p \leq n$), and $[\mu]$ is the $(\nu_p \times \nu_p)$ diagonal matrix of the ν_p positive eigenvalues of the empirical estimate of the covariance matrix of $\mathbf{X}$. The $(n_x \times \nu_p)$ matrix $[\varphi]$ consists of the associated eigenvectors such $[\varphi]^T\,[\varphi] = [I_{\nu_p}]$. The matrix $[\underline{x}]$ in $\mathbb{M}_{n_x, n_d}$ has identical columns, each being equal to the empirical estimate $\underline{\mathbf{x}} \in \mathbb{R}^{n_x}$ of the mean value of random vector $\mathbf{X}$. The columns of $[\mathbf{H}]$ are n_d independent copies of a random vector $\mathbf{H}$ with values in $\mathbb{R}^{\nu_p}$, satisfying the normalization conditions, $E\{\mathbf{H}\} = \mathbf{0}_{\nu_p}$ and $E\{\mathbf{H} \otimes \mathbf{H}\} = [I_{\nu_p}]$. The realization $[\eta_d] = [\boldsymbol{\eta}^1 \ldots \boldsymbol{\eta}^{n_d}] \in \mathbb{M}_{\nu_p, n_d}$ of $[\mathbf{H}]$ is computed by $[\eta_d] = [\mu]^{-1/2}[\varphi]^T\,([x_d] - [\underline{x}])$. The value ν_p is classically

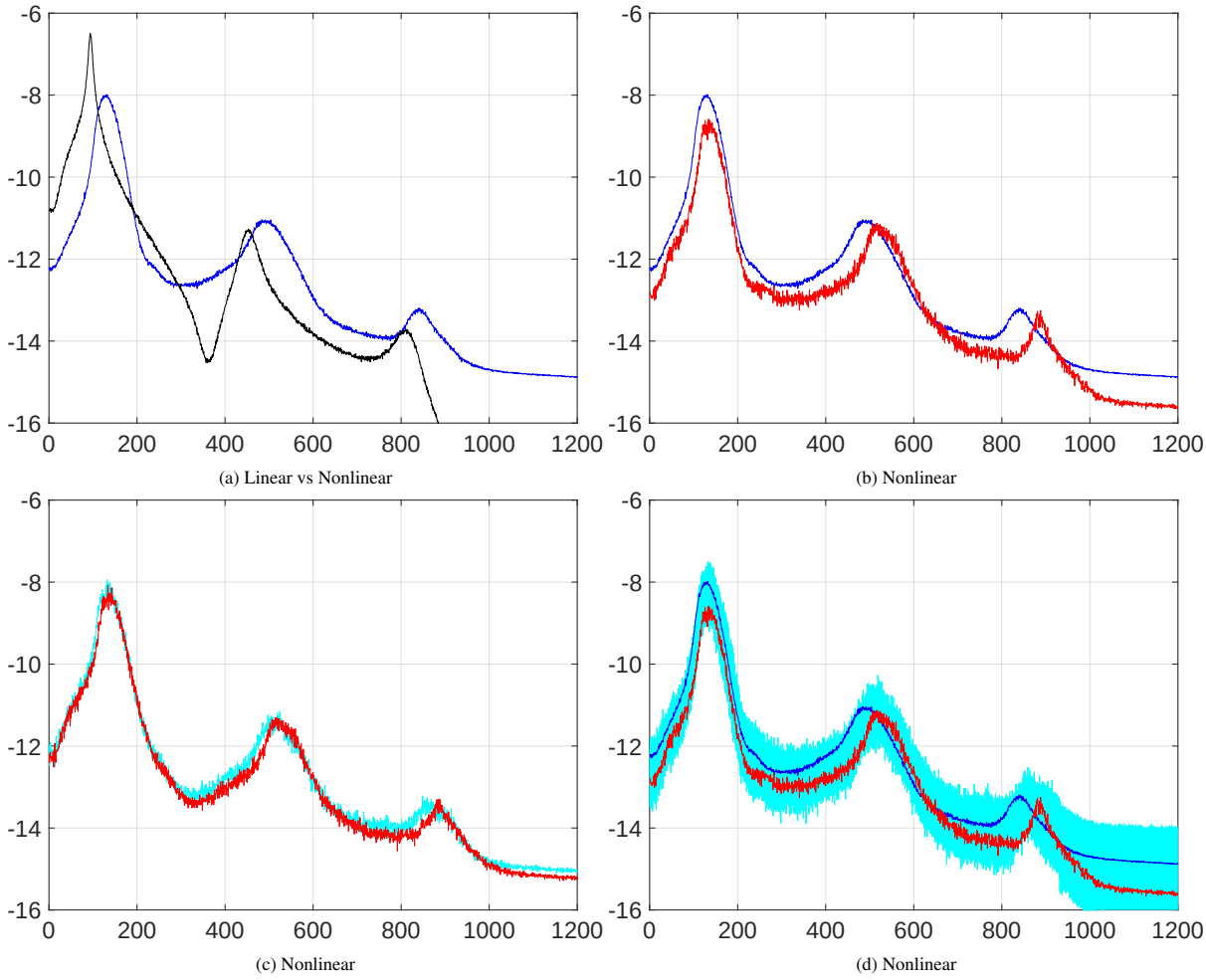

(a) Linear vs Nonlinear (b) Nonlinear

(c) Nonlinear (d) Nonlinear

Figure 17: Validation observation 1 (see legend Fig. 14)

calculated in order that the L^2- error function $\nu_p \mapsto \mathrm{err}_{\mathbf{X}}(\nu_p)$, defined by

$$\mathrm{err}_{\mathbf{X}}(\nu_p) = 1 - \frac{\sum_{\alpha=1}^{\nu_p} \mu_\alpha}{E\{\|\mathbf{X}\|^2\}}\,, \tag{A.2}$$

be smaller than $\varepsilon_{\mathrm{PCA}}$.

(v) Probability measure of $\mathbf{H}$. Let $P_{\mathbf{H}}(d\boldsymbol{\eta}) = p_{\mathbf{H}}(\boldsymbol{\eta})\, d\boldsymbol{\eta}$ be the prior probability measure on $\mathbb{R}^{\nu_p}$ of $\mathbf{H}$, whose pdf $\boldsymbol{\eta} \mapsto p_{\mathbf{H}}(\boldsymbol{\eta}) : \mathbb{R}^{\nu_p} \to \mathbb{R}^+$ is estimated by using the Gaussian kernel-density estimation (KDE) with the training dataset $\mathcal{D}_{\mathrm{train}}(\boldsymbol{\eta}) = \{\boldsymbol{\eta}^j, j = 1, \ldots, n_d\}$, involving a modification of the classical formulation [70] for which $s_{\mathrm{SB}} = \left(4/(n_d(2+\nu_p))\right)^{1/(\nu_p+4)}$ is the Silverman bandwidth. For all $\boldsymbol{\eta}$ in $\mathbb{R}^{\nu_p}$, we have

$$p_{\mathbf{H}}(\boldsymbol{\eta}) = \frac{1}{n_d} \sum_{j=1}^{n_d} \frac{1}{(\sqrt{2\pi}\,\hat{s})^{\nu_p}} \exp\left(-\frac{1}{2\hat{s}^2} \| \frac{\hat{s}}{s_{\mathrm{SB}}} \boldsymbol{\eta}^j - \boldsymbol{\eta} \|^2 \right),$$

where $\hat{s} = s_{\mathrm{SB}} \left(s_{\mathrm{SB}}^2 + (n_d - 1)/n_d\right)^{-1/2}$. With such a modification, the normalization of $\mathbf{H}$ is preserved for any value of n_d.

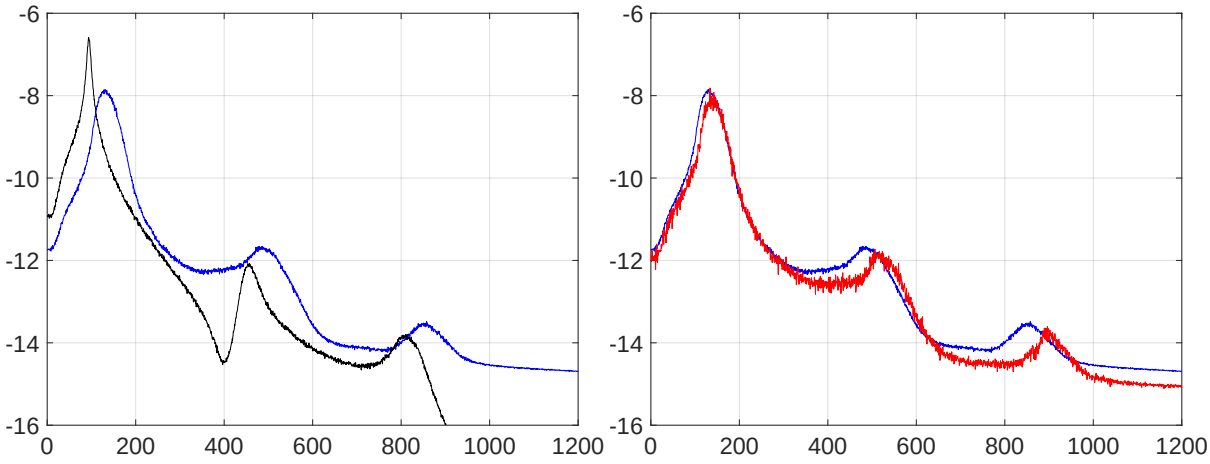

(a) Linear vs Nonlinear

(b) Nonlinear

(c) Nonlinear

(d) Nonlinear

Figure 18: Validation observation 2 (see legend Fig. 14).

(vi) Reduced-order basis using Diffusion Maps. The PLoM formulation relies on vector space $\mathbb{R}^{n_d}$ algebraic basis, constructed using the diffusion-maps basis [71]. Let $[K]$ and $[b]$ be matrices defined as $[K]_{ij} = \exp\{-(4\,\varepsilon_{\text{DM}})^{-1}\|\boldsymbol{\eta}^i - \boldsymbol{\eta}^j\|^2\}$ and $[b]_{ij} = \delta_{ij}\,b_i$ with $b_i = \sum_{j=1}^{n_d}[K]_{ij}$, where $\varepsilon_{\text{DM}} > 0$ is a smoothing parameter. Let $[\mathbb{P}] = [b]^{-1}[K]$ in $\mathbb{M}_{n_d}$, with positive entries, represents the transition matrix of a Markov chain. The eigenvalues $\lambda_1, \ldots, \lambda_{n_d}$ and associated eigenvectors $\boldsymbol{\psi}^1, \ldots, \boldsymbol{\psi}^{n_d}$ satisfy $1 = \lambda_1 > \lambda_2 \geq \ldots \geq \lambda_{n_d}$ and are computed by solving the generalized eigenvalue problem $[K]\,\boldsymbol{\psi}^\alpha = \lambda_\alpha\,[b]\,\boldsymbol{\psi}^\alpha$ with the normalization condition $\langle [b]\,\boldsymbol{\psi}^\alpha, \boldsymbol{\psi}^\beta\rangle = \delta_{\alpha\beta}$. For a given integer $\kappa \geq 0$, the diffusion-maps basis $\{\mathbf{g}^1, \ldots, \mathbf{g}^\alpha, \ldots, \mathbf{g}^{n_d}\}$ forms a vector basis of $\mathbb{R}^{n_d}$ defined by $\mathbf{g}^\alpha = \lambda_\alpha^\kappa\,\boldsymbol{\psi}^\alpha$. The reduced-order diffusion-maps basis of order m is defined as $\{\mathbf{g}^1, \ldots, \mathbf{g}^m\}$ with $[g_m] = [\mathbf{g}^1 \ldots \mathbf{g}^m] \in \mathbb{M}_{n_d,m}$. This basis depends on ε_{DM} and m. It is proven in [38] that the PLoM method does not depend on κ, which can be chosen as 0. The optimal values $m_{\text{opt}} \leq n_d$ for m and $\varepsilon_{\text{opt}} > 0$ for ε_{DM} are determined such that $1 = \lambda_1 > \lambda_2(\varepsilon_{\text{opt}}) \simeq \ldots \simeq \lambda_{m_{\text{opt}}}(\varepsilon_{\text{opt}}) \gg \lambda_{m_{\text{opt}}+1}(\varepsilon_{\text{opt}}) \geq \ldots \geq \lambda_{n_d}(\varepsilon_{\text{opt}}) > 0$, with an amplitude jump of an order of magnitude (10-fold, as demonstrated in [38]) between $\lambda_{m_{\text{opt}}}(\varepsilon_{\text{opt}})$ and $\lambda_{m_{\text{opt}}+1}(\varepsilon_{\text{opt}})$. The algorithm for estimating ε_{opt} and m_{opt} involves setting $m = \nu_p + 1$ and identifying the smallest ε_{opt} such that $\text{Jump}(\varepsilon_{\text{opt}}) \leq 0.1$.

(vii) Reduced-order representation of random matrices $[\mathbf{H}]$. The diffusion-maps vectors $\mathbf{g}^1, \ldots, \mathbf{g}^m \in \mathbb{R}^{n_d}$ span a subspace of $\mathbb{R}^{n_d}$ that characterizes, for the optimal values m_{opt} and ε_{opt} of m and ε_{DM}, the local geometry structure of dataset $\{\boldsymbol{\eta}^j, j = 1, \ldots, n_d\}$. The PLoM method introduces the $\mathbb{M}_{\nu_p,n_d}$-valued random matrix $[\mathbf{H}_m] = [\mathbf{Z}_m]\,[g_m]^T$ with

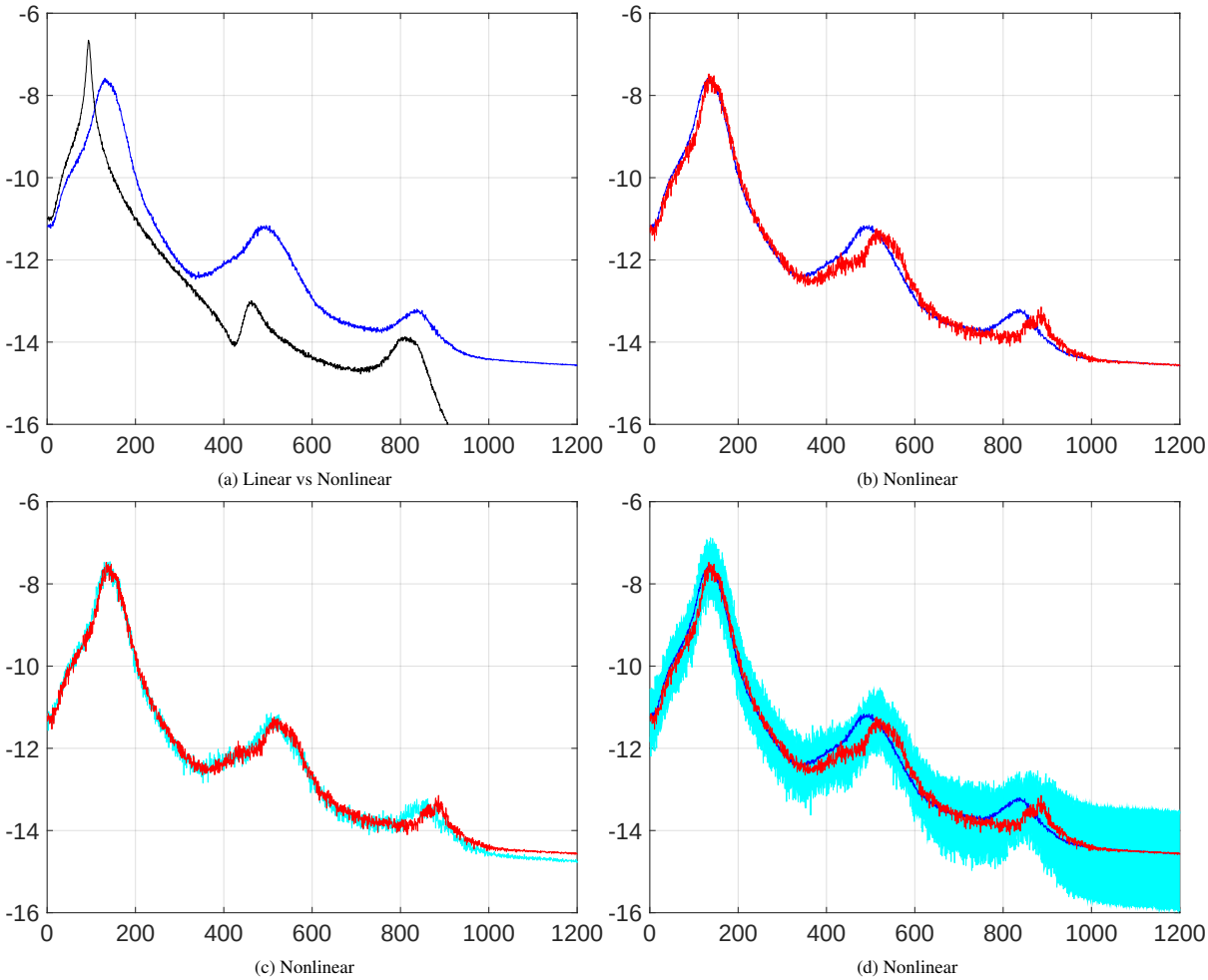

(a) Linear vs Nonlinear (b) Nonlinear

(c) Nonlinear (d) Nonlinear

Figure 19: Validation observation 3 (see legend Fig. 14).

$m \leq n_d$, corresponding to a data-reduction representation of random matrix $[\mathbf{H}]$, in which $[\mathbf{Z}_m]$ is a $\mathbb{M}_{\nu_p,m}$-valued random matrix. For generating the learned dataset, the best probability measure of $[\mathbf{H}_m]$ is obtained for $m = m_{\text{opt}}$ and by using the previously defined basis $[g_{m_{\text{opt}}}]$. For these optimal quantities m_{opt} and $[g_{m_{\text{opt}}}]$, the generator allows for computing n_{MC} realizations of $[\mathbf{Z}_{m_{\text{opt}}}]$ and therefore, for deducing the n_{MC} realizations of $[\mathbf{H}_{m_{\text{opt}}}]$.

(viii) PLoM-MCMC generator of learned realizations without imposed constraint. The MCMC generator (which is detailed in [32]) is obtained by the projection of the ISDE on the diffusion-maps basis defined in paragraph (vi). Let $\{([\mathcal{Z}(r)], [\boldsymbol{\mathcal{Y}}(r)]), r \in \mathbb{R}^+\}$ be the unique asymptotic (as $r \to +\infty$) stationary diffusion stochastic process with values in $\mathbb{M}_{\nu_p,m_{\text{opt}}} \times \mathbb{M}_{\nu_p,m_{\text{opt}}}$, representing the following reduced-order ISDE , for $r > 0$,

$$d[\mathcal{Z}(r)] = [\boldsymbol{\mathcal{Y}}(r)]dr\,,$$
$$d[\boldsymbol{\mathcal{Y}}(r)] = [\mathcal{L}([\mathcal{Z}(r)])]dr - \frac{1}{2} f_0 [\boldsymbol{\mathcal{Y}}(r)]dr + \sqrt{f_0}\,[d^r\boldsymbol{W}^{\text{wien}}(r)],$$

with $[\mathcal{Z}(0)] = [\eta_d]\,[a]$ and $[\boldsymbol{\mathcal{Y}}(0)] = [\mathbf{N}]\,[a]$, in which

$$[a] = [g_{m_{\text{opt}}}]\,([g_{m_{\text{opt}}}]^T\,[g_{m_{\text{opt}}}])^{-1} \in \mathbb{M}_{n_d,m_{\text{opt}}}\,.$$

(a) $[\mathcal{L}([\mathcal{Z}(r)])] = [L([\mathcal{Z}(r)]\,[g_{m_{\rm opt}}]^T)]\,[a]$ is a random matrix with values in $\mathbb{M}_{\nu_p,m_{\rm opt}}$. For all $[u] = [\mathbf{u}^1 \ldots \mathbf{u}^{n_d}]$ in $\mathbb{M}_{\nu_p,n_d}$ with $\mathbf{u}^j = (u_1^j, \ldots, u_{\nu_p}^j)$ in $\mathbb{R}^{\nu_p}$, the matrix $[L([u])]$ in $\mathbb{M}_{\nu_p,n_d}$ is defined, for all $k = 1, \ldots, \nu_p$ and for all $j = 1, \ldots, n_d$, by

$$[L([u])]_{kj} = \frac{1}{p(\mathbf{u}^j)}\,\{\boldsymbol{\nabla}_{\mathbf{u}^j}\, p(\mathbf{u}^j)\}_k\,, \tag{A.3}$$

$$p(\mathbf{u}^j) = \frac{1}{n_d}\sum_{j'=1}^{n_d} \exp\{-\frac{1}{2\hat{s}_{\nu_p}^2}\|\frac{\hat{s}_{\nu_p}}{s_{\nu_p}}\boldsymbol{\eta}^{j'} - \mathbf{u}^j\|^2\}\,,$$

$$\boldsymbol{\nabla}_{\mathbf{u}^j}\, p(\mathbf{u}^j) = \frac{1}{\hat{s}_{\nu_p}^2\, n_d}\sum_{j'=1}^{n_d}(\frac{\hat{s}_{\nu_p}}{s_{\nu_p}}\boldsymbol{\eta}^{j'} - \mathbf{u}^j)\, \exp\{-\frac{1}{2\hat{s}_{\nu_p}^2}\|\frac{\hat{s}_{\nu_p}}{s_{\nu_p}}\boldsymbol{\eta}^{j'} - \mathbf{u}^j\|^2\}\,.$$

(b) $[\boldsymbol{\mathcal{W}}^{\rm wien}(r)] = [\mathbf{W}^{\rm wien}(r)]\,[a]$ where $\{[\mathbf{W}^{\rm wien}(r)],\, r \in \mathbb{R}^+\}$ is the $\mathbb{M}_{\nu_p,n_d}$-valued normalized Wiener process.

(c) $[\mathbf{N}]$ is the $\mathbb{M}_{\nu_p,n_d}$-valued normalized Gaussian random matrix that is independent of process $[\mathbf{W}^{\rm wien}]$.

(d) We then have $[\mathbf{Z}_{m_{\rm opt}}] = \lim_{r\to+\infty}[\mathcal{Z}(r)]$ in probability distribution. The Störmer-Verlet scheme employed for solving the reduced-order ISDE (see [32]), allows for generating $n_{\rm MC}$ learned realizations of $[\mathbf{Z}_{m_{\rm opt}}]$. Subsequently, in parallel computation, we generate the $n_{\rm MC}$ associated learned realizations of $[\mathbf{H}_{m_{\rm opt}}]$. Each realization of $[\mathbf{Z}_{m_{\rm opt}}]$ is computed on a "worker" associated with a realization of the Wiener process $[\boldsymbol{\mathcal{W}}^{\rm wien}]$.

(e) The free parameter f_0, satisfying $0 < f_0 < 4/\hat{s}_{\nu_p}$, allows for controlling the dissipation term in the nonlinear second-order dynamic system to quickly damp the transient effects induced by the initial conditions. A commonly used value is $f_0 = 4$ (noting that $\hat{s}_{\nu_p} < 1$). Consequently, the reduced-order ISDE is solved over the interval $]0, R]$, where R depends on f_0 and represents the smallest final integration parameter allowing $[\mathbf{Z}_{m_{\rm opt}}]$ to be chosen as $[\mathcal{Z}(R)]$ while being in the stationary regime.

(ix) Projection of the target on the model in the context of incomplete data due to the partial observability. For $r = 1, \ldots, N_r$, we associate a vector $\boldsymbol{\eta}_{\rm targ}^r \in \mathbb{R}^{\nu_p}$ to $(\mathbf{o}_{\rm targ}^r, \mathbf{w}_{\rm targ}^r) \in \mathbb{R}^{n_{\rm o}+n_w}$. We then have to build a mapping that associates a vector $\boldsymbol{\eta} \in \mathbb{R}^{\nu_p}$ to each $(\mathbf{o}_{\rm id}, \mathbf{w}) \in \mathbb{R}^{n_{\rm o}+n_w}$. For any realization $\boldsymbol{\eta}$ in $\mathbb{R}^{\nu_p}$ of $\mathbf{H}$, the corresponding realization $\mathbf{x}$ of $\mathbf{X}$ is given by Eq. (A.1), $\mathbf{x} = \underline{\mathbf{x}} + [\varphi]\,[\mu]^{1/2}\,\boldsymbol{\eta}$. Since $\mathbf{x} = (\mathbf{o}, \mathbf{o}_{\rm id}, \mathbf{w})$, the extraction of $\boldsymbol{\xi} = (\mathbf{o}_{\rm id}, \mathbf{w}) \in \mathbb{R}^{n_\xi}$ with $n_\xi = n_{\rm o} + n_w$ from $\mathbf{x} \in \mathbb{R}^{n_x}$ yields

$$\boldsymbol{\xi} = \underline{\boldsymbol{\xi}} + [A_\xi]\,\boldsymbol{\eta}\ ,\ [A_\xi] = [\varphi_\xi]\,[\mu]^{1/2} \in M_{n_\xi,\nu_p}\,, \tag{A.4}$$

in which $\underline{\boldsymbol{\xi}} = (\underline{\mathbf{o}}_{\rm id}, \underline{\mathbf{w}}) \in \mathbb{R}^{n_\xi}$ and where $[\varphi_\xi] \in \mathbb{M}_{n_\xi,\nu_p}$. The matrix $[A_\xi] \in M_{n_\xi,\nu_p}$ admits a unique left pseudo-inverse $[A_\xi^{\rm inv}] \in \mathbb{M}_{\nu_p,n_\xi}$. The desired mapping is constructed by solving the equation $[A_\xi]\,\boldsymbol{\eta} = \boldsymbol{\xi} - \underline{\boldsymbol{\xi}}$ in the linear least-squares sense, which admits the unique solution $\boldsymbol{\eta} = [A_\xi^{\rm inv}]\,(\boldsymbol{\xi} - \underline{\boldsymbol{\xi}})$. We then have

$$\boldsymbol{\eta}_{\rm targ}^r = [A_\xi^{\rm inv}]\,(\boldsymbol{\xi}_{\rm targ}^r - \underline{\boldsymbol{\xi}}) \quad , \quad r \in \{1, \ldots, N_r\}\,, \tag{A.5}$$

in which $\boldsymbol{\xi}_{\rm targ}^r = (\mathbf{o}_{\rm targ}^r, \mathbf{w}_{\rm targ}^r) \in \mathbb{R}^{n_\xi}$.

(x) Learned dataset construction under constraint for $\mathbf{H}_{\rm ud}$. When imposing the constraint on $\mathbf{H}$, denoted as $\mathbf{H}_{\rm ud}$, the construction of the learned dataset $\mathcal{D}_{\rm learn}(\boldsymbol{\eta}_{\rm ud}) = \{\boldsymbol{\eta}_{\rm ud}^\ell, \ell = 1, \ldots, N_{\rm ud}\}$ for the $\mathbb{R}^{\nu_p}$-valued random variable $\mathbf{H}_{\rm ud}$ follows the Kullback-Leibler Divergence Minimum Principle (KLDMP). This principle relies on the prior pdf of $\mathbf{H}$, constructed using the training dataset $\mathcal{D}_{\rm train}(\boldsymbol{\eta}) = \{\boldsymbol{\eta}^j, j = 1, \ldots, n_d\}$, and the updated pdf of $\mathbf{H}_{\rm ud}$ using the target dataset $\mathcal{D}_{\rm targ}(\boldsymbol{\eta}_{\rm targ}) = \{\boldsymbol{\eta}_{\rm targ}^r, r = 1, \ldots, N_r\}$. The KLDMP constraints are expressed in the form of a mathematical expectation. Given that the constraints are specified by realizations forming the points of the target dataset, a weak formulation of the Fourier transform of the probability measures is employed [68].

(xi) Representation of the constraint defined by the target dataset. In [68], it is proven that the constraint defined by the target dataset $\mathcal{D}_{\rm targ}(\boldsymbol{\eta}_{\rm targ}) = \{\boldsymbol{\eta}_{\rm targ}^r, r = 1, \ldots, N_r\}$ can be written as

$$E\{\mathbf{h}^c(\mathbf{H})\} = \mathbf{b}^c \text{ on } \mathbb{R}^{N_r}\,, \tag{A.6}$$

where $\mathbf{h}^c(\boldsymbol{\eta}) = (h_1^c(\boldsymbol{\eta}), \ldots, h_{N_r}^c(\boldsymbol{\eta}))$ and $\mathbf{b}^c = (b_1^c, \ldots, b_{N_r}^c)$ are the vectors in $\mathbb{R}^{N_r}$, which are written, for $r \in \{1, \ldots, N_r\}$ and $\boldsymbol{\eta} \in \mathbb{R}^{\nu_p}$, as $h_r^c(\boldsymbol{\eta}) = \exp(-\frac{1}{\nu_p s^2} \| \boldsymbol{\eta} - \boldsymbol{\eta}_{\text{targ}}^r \|^2)$ and $b_r^c = \frac{1}{N_r} \sum_{r'=1}^{N_r} \exp(-\frac{1}{\nu_p s^2} \| \boldsymbol{\eta}_{\text{targ}}^{r'} - \boldsymbol{\eta}_{\text{targ}}^r \|^2)$, in which $s = \left(4 \left(N_r(2+\nu_p)\right)^{-1}\right)^{1/(\nu_p+4)}$.

(xii) Updated estimate using the Kullback-Leibler divergence minimum principle. The updated pdf $\boldsymbol{\eta} \mapsto p_{\mathbf{H}_{\text{ud}}}(\boldsymbol{\eta})$ on $\mathbb{R}^{\nu_p}$ of the $\mathbb{R}^{\nu_p}$-valued random variable $\mathbf{H}_{\text{ud}}$ is estimated by using the KLDMP [72, 73, 74, 39, 68]. The pdf $p_{\mathbf{H}_{\text{ud}}}$ on $\mathbb{R}^{\nu_p}$, which satisfies the constraint defined by Eq. (A.6) and which is closest to $p_{\mathbf{H}}$, is the solution of the following optimization problem,

$$p_{\mathbf{H}_{\text{ud}}} = \arg \min_{p \in C_{\text{ad},p}} \int_{\mathbb{R}^{\nu_p}} p(\boldsymbol{\eta}) \log \left(\frac{p(\boldsymbol{\eta})}{p_{\mathbf{H}}(\boldsymbol{\eta})} \right) d\boldsymbol{\eta}\,, \tag{A.7}$$

where $C_{\text{ad},p} = \{\boldsymbol{\eta} \mapsto p(\boldsymbol{\eta}) : \mathbb{R}^{\nu_p} \to \mathbb{R}^+ \,, \int_{\mathbb{R}^{\nu_p}} p(\boldsymbol{\eta})\, d\boldsymbol{\eta} = 1 \;\; \int_{\mathbb{R}^{\nu_p}} \mathbf{h}^c(\boldsymbol{\eta})\, p(\boldsymbol{\eta})\, d\boldsymbol{\eta} = \mathbf{b}^c\}$ is the admissible set.

(xiii) Methodology for solving the optimization problem. The constraints within the admissible set $C_{\text{ad},p}$ are incorporated by introducing Lagrange multipliers. The updated pdf $p_{\mathbf{H}_{\text{ud}}}$ is constructed as the limit of a sequence $\{p_{\mathbf{H}_\lambda}\}_\lambda$ of pdfs for a sequence $\{\mathbf{H}_\lambda\}_\lambda$ of $\mathbb{R}^{\nu_p}$-valued random variables $\mathbf{H}_\lambda$, dependent on a Lagrange multiplier $\boldsymbol{\lambda} \in C_{\text{ad},\lambda} \subset \mathbb{R}^{N_r}$. The limit of the sequence in $\boldsymbol{\lambda}$ is denoted as $\boldsymbol{\lambda}^{\text{sol}}$, satisfying $\mathbf{H}_{\text{ud}} = \mathbf{H}_{\boldsymbol{\lambda}^{\text{sol}}}$. In Theorem 3 of [68], it is proven that $\boldsymbol{\lambda}^{\text{sol}}$ is the unique solution in $C_{\text{ad},\lambda}$ of the convex optimization problem, $\boldsymbol{\lambda}^{\text{sol}} = \arg \min_{\lambda \in C_{\text{ad},\lambda}} \Gamma(\boldsymbol{\lambda})$ where Γ is the strictly convex function on $C_{\text{ad},\lambda}$ with first and second derivatives given by,

$$\boldsymbol{\Gamma}'(\boldsymbol{\lambda}) = \mathbf{b}^c - E\{\mathbf{h}^c(\mathbf{H}_\lambda)\} \in \mathbb{R}^{N_r}\,,$$

$$[\Gamma''(\boldsymbol{\lambda})] = [\text{cov}\{\mathbf{h}^c(\mathbf{H}_\lambda)\}] \in \mathbb{M}_{N_r}^+\,.$$

Here $[\Gamma''(\boldsymbol{\lambda})]$ is the positive-definite covariance matrix of $\mathbf{h}^c(\mathbf{H}_\lambda)$. The vector $\boldsymbol{\lambda}^{\text{sol}}$ is the unique solution in $\boldsymbol{\lambda}$ of $\boldsymbol{\Gamma}'(\boldsymbol{\lambda}) = \mathbf{0}_{N_r}$ and is obtained using the Newton iterative method. At each iteration i, $\boldsymbol{\lambda}^{i+1}$ is computed as a function of $\boldsymbol{\lambda}^i$ by

$$\boldsymbol{\lambda}^{i+1} = \boldsymbol{\lambda}^i - \alpha_{\text{relax}}(i)\, [\Gamma''(\boldsymbol{\lambda}^i)]^{-1}\, \boldsymbol{\Gamma}'(\boldsymbol{\lambda}^i) \quad , \quad i \geq 0\,,$$

with the initial value $\boldsymbol{\lambda}^0 = \mathbf{0}_{N_r}$. In this equation, the positive coefficient $\alpha_{\text{relax}}(i)$, a relaxation parameter (less than 1), controls the convergence of the iteration algorithm. Given $i_2 \geq 2$, β_1, and β_2 such that $0 < \beta_1 < \beta_2 \leq 1$, α_i is defined for $i \leq i_2$ as $\alpha_i = \beta_1 + (\beta_2 - \beta_1)(i-1)/(i_2 - 1)$, and for $i > i_2$ as $\alpha_i = \beta_2$. The convergence of the iteration algorithm is controlled by the error function $i \mapsto \text{err}(i)$ defined by

$$\text{err}(i) = \|\mathbf{b}^c - E\{\mathbf{h}^c(\mathbf{H}_{\lambda^i})\}\| / \|\mathbf{b}^c\|\,. \tag{A.8}$$

At each iteration i, $E\{\mathbf{h}^c(\mathbf{H}_{\lambda^i})\}$ and $[\text{cov}\{\mathbf{h}^c(\mathbf{H}_{\lambda^i})\}]$ are estimated using $N_{\text{ud}} = n_{\text{MC}} \times n_d$ learned realizations with the MCMC generator of $[\mathbf{H}_{\lambda^i}]$ defined in (viii). In this generator, the mapping $[L]$, defined by Eq. (A.3), is replaced by the following,

$$[L_{\lambda^i}([u])]_{kj} = \frac{1}{p(\mathbf{u}^j)} \{\boldsymbol{\nabla}_{\mathbf{u}^j} p(\mathbf{u}^j)\}_k - \{[\boldsymbol{\nabla}_{\mathbf{u}^j} \mathbf{h}^c(\mathbf{u}^j)]\, \boldsymbol{\lambda}^i\}_k. \tag{A.9}$$

References

[1] G. A. Brès, P. Jordan, V. Jaunet, M. Le Rallic, A. V. Cavalieri, A. Towne, S. K. Lele, T. Colonius, O. T. Schmidt, Importance of the nozzle-exit boundary-layer state in subsonic turbulent jets, Journal of Fluid Mechanics 851 (2018) 83–124. doi:10.1017/jfm.2018.476.

[2] Q. Dang Le, R. Mereu, G. Besagni, V. Dossena, F. Inzoli, Computational fluid dynamics modeling of flashing flow in convergent-divergent nozzle, Journal of Fluids Engineering 140 (10) (2018) 101102. doi:10.1115/1.4039908.

[3] T. Trummler, S. J. Schmidt, N. A. Adams, Investigation of condensation shocks and re-entrant jet dynamics in a cavitating nozzle flow by large-eddy simulation, International Journal of Multiphase Flow 125 (2020) 103215. doi:10.1016/j.ijmultiphaseflow.2020.1032.

[4] J. C. French, Nozzle acoustic dynamics and stability modeling, Journal of Propulsion and Power 27 (6) (2011) 1266–1275. doi:10.2514/1.B34239.

[5] G. A. Brès, S. K. Lele, Modelling of jet noise: a perspective from large-eddy simulations, Philosophical Transactions of the Royal Society A 377 (2159) (2019) 20190081. doi:10.1098/rsta.2019.0081.

[6] N. P. Breen, K. K. Ahuja, Supersonic jet noise source distributions, The Journal of the Acoustical Society of America 150 (3) (2021) 2193–2203. doi:10.1121/10.0006381.

[7] K. Volkov, V. Emel'yanov, P. Chernyshov, Flow dynamics and acoustics of the gas jet emanating from a conical nozzle into an immersed space, Journal of Engineering Physics and Thermophysics 95 (2) (2022) 409–420. doi:10.1007/s10891-022-02495-x.
[8] Y. Jia-hui, W. Ke, G. Xiu-cong, Dynamic simulation of nozzle structure based on thermal-fluid-solid coupling analysis, Journal of Physics: Conference Series 2472 (2023) 012065. doi:10.1088/1742-6596/2472/1/012065.
[9] R. Bunker, A. Prince, Hybrid rocket motor nozzle material predictions and results, in: 28th Joint Propulsion Conference and Exhibit, 1992, p. 3591. doi:10.2514/6.1992-3591.
[10] D. Bianchi, F. Nasuti, Numerical analysis of nozzle material thermochemical erosion in hybrid rocket engines, Journal of Propulsion and Power 29 (3) (2013) 547–558. doi:10.2514/1.B34813.
[11] S. Mungiguerra, G. D. Di Martino, R. Savino, L. Zoli, L. Silvestroni, D. Sciti, Characterization of novel ceramic composites for rocket nozzles in high-temperature harsh environments, International Journal of Heat and Mass Transfer 163 (2020) 120492. doi:10.1016/j.ijheatmasstransfer.2020.120492.
[12] R. A. Newton, Free vibrations of rocket nozzles., AIAA Journal 4 (7) (1966) 1303–1305. doi:10.2514/3.3666.
[13] L. Garelli, R. R. Paz, M. A. Storti, Fluid–structure interaction study of the start-up of a rocket engine nozzle, Computers & Fluids 39 (7) (2010) 1208–1218. doi:10.1016/j.compfluid.2010.03.005.
[14] X. Zhao, S. Bayyuk, S. Zhang, Aeroelastic response of rocket nozzles to asymmetric thrust loading, Computers & Fluids 76 (2013) 128–148. doi:10.1016/j.compfluid.2013.01.022.
[15] J. K. Ignatius, R. V. Venkata, S. Sathiyavageeswaran, Investigation on the vibration response to high-intensity pressure waves during a solid rocket motor operation, in: Advances in Rotor Dynamics, Control, and Structural Health Monitoring: Select Proceedings of ICOVP 2017, Springer, 2020, pp. 227–255. doi:10.1007/978-981-15-5693-7_17.
[16] S. Jack, M. Oschwald, T. Eggers, Mechanisms contributing to the dynamic stability of a flexible subscale rocket nozzle, Journal of Propulsion and Power (2023) 1–11doi:10.2514/1.B39178.
[17] J. M. Seiner, M. Gilinsky, Nozzle thrust optimization while reducing jet noise, AIAA journal 35 (3) (1997) 420–427. doi:10.2514/2.130.
[18] H. Ogawa, R. R. Boyce, Nozzle design optimization for axisymmetric scramjets by using surrogate-assisted evolutionary algorithms, Journal of Propulsion and Power 28 (6) (2012) 1324–1338. doi:10.2514/1.B34482.
[19] X.-Y. Liu, M. Cheng, Y.-Z. Zhang, J.-P. Wang, Design and optimization of aerospike nozzle for rotating detonation engine, Aerospace Science and Technology 120 (2022) 107300. doi:10.1016/j.ast.2021.107300.
[20] J.-G. Ye, S.-S. Xu, H.-F. Huang, Y.-J. Zhao, W. Zhou, Y.-L. Zhang, Optimization design of nozzle structure inside boiler based on orthogonal design, Processes 11 (10) (2023) 2923. doi:10.3390/pr11102923.
[21] S. Patil, Investigation of nozzle shape, number of nozzles and nozzle inclination angle and its optimization, Tuijin Jishu/Journal of Propulsion Technology 44 (2023) 1266–1279. doi:10.52783/tjjpt.v44.i4.1008.
[22] P. Wang, W. Yang, Pneumatic rotary nozzle structure optimization design and airflow characteristics analysis, Advances in Mechanical Engineering 15 (2023) 1–15. doi:10.1177/16878132231195016.
[23] Q.-Y. Chen, D. Gottlieb, J. S. Hesthaven, Uncertainty analysis for the steady-state flows in a dual throat nozzle, Journal of Computational Physics 204 (1) (2005) 378–398. doi:10.1016/j.jcp.2004.10.019.
[24] C. J. Roy, M. S. Balch, A holistic approach to uncertainty quantification with application to supersonic nozzle thrust, International Journal for Uncertainty Quantification 2 (4) (2012) 363–381. doi:10.1615/Int.J.UncertaintyQuantification.2012003562.
[25] W. Xie, Y. Yang, S. Meng, T. Peng, J. Yuan, F. Scarpa, C. Xu, H. Jin, Probabilistic reliability analysis of carbon/carbon composite nozzle cones with uncertain parameters, Journal of Spacecraft and Rockets 56 (6) (2019) 1765–1774. doi:10.2514/1.A34392.
[26] B. Yue, G. Zhu, X. Cao, S. Qiao, N. Guo, Y. An, Uncertainty analysis of the influence of delivery system nozzle structure on fluid-thermal coupling in casting molten pool, International Journal of Material Forming 14 (2021) 593–605. doi:10.1007/s12289-020-01549-w.
[27] A. Talwalkar, S. Kumar, H. Rowley, Large-scale manifold learning, in: 2008 IEEE Conference on Computer Vision and Pattern Recognition, IEEE, 2008, pp. 1–8. doi:10.1109/CVPR.2008.4587670.
[28] D. Gorissen, I. Couckuyt, P. Demeester, T. Dhaene, K. Crombecq, A surrogate modeling and adaptive sampling toolbox for computer based design, Journal of Machine Learning Research 11 (68) (2010) 2051–2055.
[29] A. C. Öztireli, M. Alexa, M. Gross, Spectral sampling of manifolds, ACM Transactions on Graphics (TOG) 29 (6) (2010) 1–8. doi:10.1145/1882261.1866190.
[30] M. Transtrum, P. Qiu, Model reduction by manifold boundaries, Physical review letters 113 (2014) 098701. doi:10.1103/PhysRevLett.113.098701.
[31] Y. Marzouk, T. Moselhy, M. Parno, A. Spantini, Sampling via measure transport: An introduction, Handbook of uncertainty quantification (2016) 1–41doi:10.1007/978-3-319-11259-6_23-1.
[32] C. Soize, R. Ghanem, Data-driven probability concentration and sampling on manifold, Journal of Computational Physics 321 (2016) 242–258. doi:10.1016/j.jcp.2016.05.044.
[33] M. D. Parno, Y. M. Marzouk, Transport map accelerated markov chain Monte Carlo, SIAM/ASA Journal on Uncertainty Quantification 6 (2) (2018) 645–682. doi:10.1137/17M1134640.
[34] G. Perrin, C. Soize, N. Ouhbi, Data-driven kernel representations for sampling with an unknown block dependence structure under correlation constraints, Computational Statistics & Data Analysis 119 (2018) 139–154. doi:10.1016/j.csda.2017.10.005.
[35] A. Holiday, M. Kooshkbaghi, J. Bello-Rivas, C. Gear, A. Zagaris, Y. Kevrekidis, Manifold learning for parameter reduction, Journal of Computational Physics 392 (2019) 419–431. doi:10.1016/j.jcp.2019.04.015.
[36] M.-J. Azzi, C. Ghnatios, P. Avery, C. Farhat, Acceleration of a physics-based machine learning approach for modeling and quantifying model-form uncertainties and performing model updating, Journal of Computing and Information Science in Engineering 23 (1) (2022) 011009. doi:10.1115/1.4055546.
[37] A. Yousefpour, M. Shishehbor, Z. Zanjani Foumani, R. Bostanabad, Unsupervised Anomaly Detection via Nonlinear Manifold Learning, Journal of Computing and Information Science in Engineering (2023) 1–37arXiv:https://asmedigitalcollection.asme.org/computingengineering/article-pdf/doi/10.1115/1.4063642/7047921/jcise-23-1278.pdf, doi:10.1115/1.4063642.

URL https://doi.org/10.1115/1.4063642
[38] C. Soize, R. Ghanem, Probabilistic learning on manifolds, Foundations of Data Science 2 (3) (2020) 279–307. doi:10.3934/fods.2020013.
[39] C. Soize, R. Ghanem, Physics-constrained non-Gaussian probabilistic learning on manifolds, International Journal for Numerical Methods in Engineering 121 (1) (2020) 110–145. doi:10.1002/nme.6202.
[40] C. Soize, R. Ghanem, Probabilistic-learning-based stochastic surrogate model from small incomplete datasets for nonlinear dynamical systems,, Computer Methods in Applied Mechanics and Engineering 418 (2023) 116498. doi:10.1016/j.cma.2023.116498.
[41] R. Ghanem, C. Soize, Probabilistic nonconvex constrained optimization with fixed number of function evaluations, International Journal for Numerical Methods in Engineering 113 (4) (2018) 719–741. doi:10.1002/nme.5632.
[42] R. Ghanem, C. Soize, C. Safta, X. Huan, G. Lacaze, J. C. Oefelein, H. N. Najm, Design optimization of a scramjet under uncertainty using probabilistic learning on manifolds, Journal of Computational Physics 399 (2019) 108930. doi:10.1016/j.jcp.2019.108930.
[43] E. Capiez-Lernout, C. Soize, Nonlinear stochastic dynamics of detuned bladed disks with uncertain mistuning and detuning optimization using a probabilistic machine learning tool, International Journal of Non-Linear Mechanics 143 (2022) 104023. doi:10.1016/j.ijnonlinmec.2022.104023.
[44] J. O. Almeida, F. A. Rochinha, A probabilistic learning approach applied to the optimization of wake steering in wind farms, Journal of Computing and Information Science in Engineering 23 (1) (2023) 011003. doi:10.1115/1.4054501.
[45] C. Farhat, R. Tezaur, T. Chapman, P. Avery, C. Soize, Feasible probabilistic learning method for model-form uncertainty quantification in vibration analysis, AIAA Journal 57 (11) (2019) 4978–4991. doi:10.2514/1.J057797.
[46] C. Safta, R. G. Ghanem, M. J. Grant, M. Sparapany, H. N. Najm, Trajectory design via unsupervised probabilistic learning on optimal manifolds, Data-Centric Engineering 3 (2022) e26. doi:10.1017/dce.2022.26.
[47] O. Ezvan, C. Soize, C. Desceliers, R. Ghanem, Updating an uncertain and expensive computational model in structural dynamics based on one single target frf using a probabilistic learning tool, Computational Mechanics 71 (2023) 1161–1177. doi:10.1007/s00466-023-02301-2.
[48] K. Zhong, J. G. Navarro, S. Govindjee, G. G. Deierlein, Surrogate modeling of structural seismic response using Probabilistic Learning on Manifolds, Earthquake Engineering and Structural Dynamics 52 (8) (2023) 2407–2428. doi:10.1002/eqe.3839.
[49] J. L. Doob, Stochastic processes, John Wiley & Sons, New York, 1953.
[50] I. I. Guikhman, A. Skorokhod, Introduction à la Théorie des Processus Aléatoires, Edition Mir, 1980.
[51] P. Krée, C. Soize, Mathematics of Random Phenomena, Reidel Pub. Co, 1986, (first published by Bordas in 1983 and also published by Springer Science & Business Media in 2012).
[52] C. Soize, Uncertainty Quantification. An Accelerated Course with Advanced Applications in Computational Engineering, Springer, New York, 2017. doi:10.1007/978-3-319-54339-0.
[53] C. Soize, An overview on uncertainty quantification and probabilistic learning on manifolds in multiscale mechanics of materials, Mathematics and Mechanics of Complex Systems 11 (1) (2023) 87–174. doi:10.2140/memocs.2023.11.87.
[54] A. Leissa, Vibration of Shells, Acoustic Society of America, Publications on Acoustics (originally published in 1973, NASA SP-288), 1973.
[55] R. Ohayon, C. Soize, Structural Acoustics and Vibration: Mechanical Models, Variational Formulations and Discretization, Academic Press, San Diego, London, 1998.
[56] K. J. Bathe, E. L. Wilson, Numerical Methods in Finite Element Analysis, Prentice-Hall, New York, 1976.
[57] E. Capiez-Lernout, C. Soize, M. Mbaye, Mistuning analysis and uncertainty quantification of an industrial bladed disk with geometrical nonlinearity, Journal of Sound and Vibration 356 (10) (2015) 124–143. doi:10.1016/j.jsv.2015.07.006.
[58] M. Crisfield, Non-linear finite element analysis of solids and structures, Vol.1: essentials, John Wiley and Sons, Chichester, 1997.
[59] R. De Borst, M. Crisfield, J. Remmers, C. V. Verhoosel, Non-Linear Finite Element Analysis of Solids and Structures, Second Edition, Wiley, 2012. doi:10.1002/9781118375938.
[60] E. Capiez-Lernout, C. Soize, M.-P. Mignolet, Post-buckling nonlinear static and dynamical analyses of uncertain cylindrical shells and experimental validation, Computer Methods in Applied Mechanics and Engineering 271 (2014) 210–230. doi:10.1016/j.cma.2013.12.011.
[61] E. Capiez-Lernout, C. Soize, An improvement of the uncertainty quantification in computational structural dynamics with nonlinear geometrical effects, International Journal for Uncertainty Quantification 7 (1) (2017) 83–98. doi:10.1615/Int.J.UncertaintyQuantification.2016019141.
[62] A. Picou, E. Capiez-Lernout, C. Soize, M. Mbaye, Robust dynamic analysis of detuned-mistuned rotating bladed disks with geometric nonlinearities, Computational Mechanics 65 (3) (2020) 711–730. doi:10.1007/s00466-019-01790-4.
[63] R. O'Leary, J. Beck, Nozzle design, Tech. rep., Boeing Engineering, Spring 1992 Issue (1992).
[64] C. Hillegass, Rocket motor nozzle, Tech. rep., Williams Honors College, Honors Research Projects 1135. (2020).
[65] C. Tam, Jet noise : Since 1952, Theoretical and Computational Fluid Dynamics 10 (1998) 393–405.
[66] M. Shinozuka, Simulation of multivariate and multidimensional random processes, The Journal of the Acoustical Society of America 49 (1B) (1971) 357–368. doi:10.1121/1.1912338.
[67] F. Poirion, C. Soize, Numerical methods and mathematical aspects for simulation of homogeneous and non homogeneous Gaussian vector fields, in: P. Krée, W. Wedig (Eds.), Probabilistic Methods in Applied Physics, Springer-Verlag, Berlin, 1995, pp. 17–53. doi:10.1007/3-540-60214-3-50.
[68] C. Soize, Probabilistic learning constrained by realizations using a weak formulation of fourier transform of probability measures, Computational Statistics 38 (4) (2023) 1879–1925. doi:10.1007/s00180-022-01300-w.
[69] C. Soize, R. Ghanem, Probabilistic learning on manifolds (PLoM) with partition, International Journal for Numerical Methods in Engineering 123 (1) (2022) 268–290. doi:10.1002/nme.6856.
[70] A. Bowman, A. Azzalini, Applied Smoothing Techniques for Data Analysis: The Kernel Approach With S-Plus Illustrations, Vol. 18, Oxford University Press, Oxford: Clarendon Press, New York, 1997. doi:10.1007/s001800000033.
[71] R. Coifman, S. Lafon, A. Lee, M. Maggioni, B. Nadler, F. Warner, S. Zucker, Geometric diffusions as a tool for harmonic analysis and structure definition of data: Diffusion maps, PNAS 102 (21) (2005) 7426–7431. doi:10.1073/pnas.0500334102.
[72] S. Kullback, R. A. Leibler, On information and sufficiency, The Annals of Mathematical Statistics 22 (1) (1951) 79–86. doi:10.1214/aoms/1177729694.
[73] J. N. Kapur, H. K. Kesavan, Entropy Optimization Principles with Applications, Academic Press, San Diego, 1992.

[74] T. M. Cover, J. A. Thomas, Elements of Information Theory, Second Edition, John Wiley & Sons, Hoboken, 2006.